

DTIC FILE COPY

5329-AN-01

(2)

ELECTRICAL IGNITION OF HAN-BASED LIQUID PROPELLANTS
Final Technical Report

AD-A223 272

by

G. Klingenberg
(Principal Investigator)

and

H.J. Frieske and H. Rockstroh

January 1990

DTIC
ELECTE
JUN 15 1990
S B D
Q10

United States Army
EUROPEAN RESEARCH OFFICE OF THE U.S. ARMY
London England

CONTRACT NUMBER DAJA 45 - 86 - C - 0029

Fraunhofer Gesellschaft e.V.
Leonrodstrasse 54, D-8000 München 19, Germany

Approved for Public Release; distribution unlimited

*Original contains color
plates: All DTIC reproductions
will be in black and
white*

90 06 1 015

REPORT DOCUMENTATION PAGE

1a. REPORT SECURITY CLASSIFICATION Unclassified			1b. RESTRICTIVE MARKINGS		
2a. SECURITY CLASSIFICATION AUTHORITY			3. DISTRIBUTION / AVAILABILITY OF REPORT Approved for public release; distribution unlimited		
2b. DECLASSIFICATION / DOWNGRADING SCHEDULE			4. PERFORMING ORGANIZATION REPORT NUMBER(S)		
5. MONITORING ORGANIZATION REPORT NUMBER(S) R&D 5329-AN-01			6a. NAME OF PERFORMING ORGANIZATION Fraunhofer-Institut für Kurzzeit- dynamik, Ernst-Mach-Institut (EMI-AFB)		
6b. ADDRESS (City, State, and ZIP Code) Hauptstrasse 18 D-7858 Weil am Rhein, FRG			7a. NAME OF MONITORING ORGANIZATION USARDSG-UK		
7b. ADDRESS (City, State, and ZIP Code) Box 65 FPO New York 09510-1500			8a. NAME OF FUNDING / SPONSORING ORGANIZATION USARDSG-UK		
8b. OFFICE SYMBOL (if applicable)			9. PROCUREMENT INSTRUMENT IDENTIFICATION NUMBER DAJA 45-86-C-0029		
8c. ADDRESS (City, State, and ZIP Code) Box 65 FPO New York 09510-1500			10. SOURCE OF FUNDING NUMBERS		
			PROGRAM ELEMENT NO.	PROJECT NO.	TASK NO.
			WORK UNIT ACCESSION NO.		
11. TITLE (Include Security Classification) (U) Electrical Ignition of HAN-Based Liquid Propellants					
12. PERSONAL AUTHOR(S) G. Klingenberg (Principal Investigator), H.-J. Frieske, H. Rockstroh					
13a. TYPE OF REPORT Final Technical		13b. TIME COVERED FROM Oct. 86 TO Dec. 89		14. DATE OF REPORT (Year, Month, Day) 90/1/4	
				15. PAGE COUNT 85	
16. SUPPLEMENTARY NOTATION					
17. COSATI CODES			18. SUBJECT TERMS (Continue on reverse if necessary and identify by block number)		
FIELD	GROUP	SUB-GROUP	(U) Guns; (U) Liquid Monopropellants; (U) Electrical Ignition; (U) Combustion; (U) HAN;		
19	06		(U) Regenerative		
21	01				
19. ABSTRACT (Continue on reverse if necessary and identify by block number) The feasibility of arcless ignition in a 2 cm ³ igniter element was demonstrated in a vented chamber and in a 30-mm regenerative liquid propellant gun. The igniter consists of a center electrode separated from a more or less conically shaped vented outer electrode by a hollow cylindrical insulator. Simple steady-state potential field calculations were used to optimize the electrode and cavity geometries. The energy transfer to the igniter is determined mainly by polarity, electrode surface area and charge voltage. Stronger confinement of the liquid propellant igniter charge will accelerate the ignition process. Scanning electron microscopy (SEM) and x-ray microanalysis show that ignition is affected by the chemical and physical characteristics of the electrode surface. Preliminary tests with multi-channel IR-spectrometry for recording the transient ignition reactions were also performed. (J25) ✓					
20. DISTRIBUTION / AVAILABILITY OF ABSTRACT <input checked="" type="checkbox"/> UNCLASSIFIED/UNLIMITED <input type="checkbox"/> SAME AS RPT <input type="checkbox"/> DTIC USERS			21. ABSTRACT SECURITY CLASSIFICATION Unclassified		
22a. NAME OF RESPONSIBLE INDIVIDUAL Dr. R. Reichenbach			22b. TELEPHONE (Include Area Code) 071-409-4485		22c. OFFICE SYMBOL AMXSN-UK-RA

TABLE OF CONTENTS

	<u>Page</u>
1. INTRODUCTION	4
1.1 Scope of Project	4
1.2 Background	5
1.2.1 Electrical Ignition	6
1.2.2 Computer Aided Igniter Design	8
2. EXPERIMENTAL	9
2.1 EMI-AFB Ignition Test Fixture 1	9
2.1.1 Igniter Mount Assembly	11
2.1.2 Electrode Configurations	15
2.1.2.1 EMI-AFB Type "BRL(m/s) "	17
2.1.2.2 Configurations EMI-AFB-1 and EMI-AFB-2	18
2.1.2.3 Configurations EMI-AFB-3 and EMI-AFB-4	20
2.1.2.4 Configuration DNAG-EMI-AFB-5	21
2.2 EMI-AFB Ignition Test Fixture 2	23
2.3 Electrical Power Supply	24
2.4 Numerical Calculations	25
2.5 30-mm RLPG Simulator	25
2.6 IR Spectroscopy	27
3. RESULTS	27
3.1 EMI-AFB Ignition Test Fixture 1	28
3.1.1 Electrical Characteristics	36
3.1.2 Effect of Chamber Volume	46
3.1.3 Effect of Vent Diameter	48
3.1.4 Effect of Polarity/Voltage	49
3.1.5 Effect of Igniter Geometry	51
3.1.5.1 Theoretical	51
3.1.5.2 Empirical	54
3.1.6 Effect of Electrode Surface	61

TABLE OF CONTENTS (Continued)

	<u>Page</u>
3.2 EMI-AFB Ignition Test Fixture 2	63
3.3 30-mm RLPG Test Firings	65
3.4 IR Spectroscopy	68
4. CONCLUSIONS	72
5. REFERENCES	74



Accession For	
NTIS GRA&I	<input checked="" type="checkbox"/>
DTIC TAB	<input type="checkbox"/>
Unannounced	<input type="checkbox"/>
Justification	
By _____	
Distribution/	
Availability Codes	
Dist	Avail and/or Special
A-1	

1. INTRODUCTION

1.1 Scope of the Project

The objectives of the research project reviewed herein were originally

- to investigate various means of electrical ignition of LGP 1846,
- to develop quantitative ignition criteria,
- to achieve reproducible igniter output energies,
- to obtain igniter energy effluxes capable of starting the regenerative process and producing self-sustained combustion in a regenerative liquid propellant gun (RLPG),
- to scale the ignition to larger volumes.

The last two of the items listed above were later narrowed into one, and restated as

- determine an optimized igniter configuration and test in a 30-mm RLPG.

During the course of the work the scope of the project was further revised and broadened to include:

- Species identification of reaction products by (mass) spectrometer.
- Determine if electrostatic potential field calculations serve as useful design guidelines.
- Determine if scanning electron microscope data and x-ray microanalysis of the electrode surface can serve as useful igniter design guidelines. The data base should include three different surface roughnesses tested at both positive and negative center electrode polarity.

This work conducted at the Ernst-Mach-Institut (EMI-AFB) is part of a three years research effort ultimately directed at designing and constructing a working electric igniter system for regenerative liquid propellant guns. Whereas the General Electric Company has developed a two-stage electric arc igniter, the Ballistic Research Laboratory (BRL) and the Ernst-Mach-Institut have focussed on arcless ignition. The EMI research program is based on initial studies conducted at BRL.

The two-stage design principle chosen at General Electric was developed from the "plasma plug" igniters studied by Weinberg et al. [1-3]. In the GE and in a later BRL igniter [4] a small primary

volume of 0.5 cm^3 liquid propellant is ignited by electric arc, the resultant hot combustion gases are vented into a second, larger chamber, which acts as a reservoir for the main body of liquid propellant. This concept has been demonstrated successfully; however, substantial material attrition, such as electrode pitting, is an issue in arc ignition.

The prospects for arcless ignition of HAN-based liquid propellants, especially LGP 1845 and LGP 1846, were initially assessed at BRL [4-6] with an igniter shown schematically in Figure 1. The liquid propellant is stored in a cavity of about 2 cm^3 volume formed by the insulator and the electrodes. The center electrode protrudes into the cavity/reservoir across from the exit vent. The gas efflux from the vent is collected in an adjacent chamber. Although the results were not entirely satisfactory [6] (low reproducibility), this concept seemed promising enough to warrant further studies which are reviewed in this report.

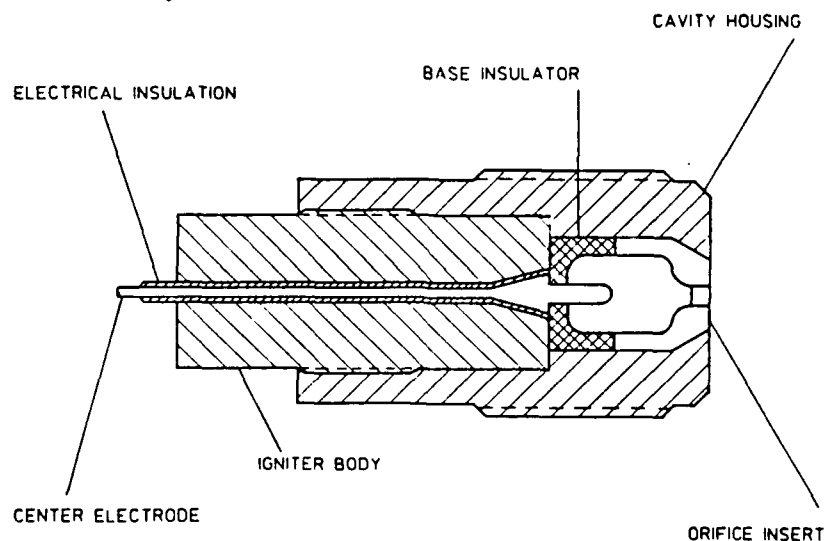


Fig. 1. Basic BRL single-stage igniter system

1.2 Background

The liquid monopropellant gun concept has been studied over the past three decades at various levels of intensity. International efforts have been gaining momentum in the last years with the United States leading the field. Research programs are also extant in England, France, Germany, and more recently in Japan.

At present the regenerative injection principle is favored over the alternative bulk loading principle throughout the research community. Bulk loading systems have not shown satisfactory reproducibility and controllability in their interior ballistic performance.

Moreover, the prospects for improvement of the technology are rated low [7].

The igniter of a regenerative liquid propellant gun (RLPG) must fulfill two functions, i.e.,

- (a) set in motion the injection (regenerative) piston to start fuel injection into the combustion chamber,
- (b) ignite the injected fuel and enable self-sustained combustion.

This requires a certain amount of energy to be released on the part of the ignition system, which depends upon the caliber of the weapon. Hitherto, the experimental RLPG simulators were in most cases equipped with pyrotechnic solid propellant igniters, since the behavior of these systems is well known. In future applications, however, liquid propellant (LP) will likely take the place of the solid propellant in ignition. One important reason is logistics; namely, it is advantageous to use only one type of propellant [8].

Of the many injection techniques considered in the last years [8] electrical ignition has received the most attention. Basically, there are two kinds of electrical ignition:

- "electrochemical" or "arcless" ignition,
- "spark" or "arc" ignition.

Electrochemical ignition requires electrically conducting propellants such as the HAN-based LGP 1846. Arc ignition is indicated, for example, with the non-electrolytic organic nitrate ester propellants such as nitromethane. Drawbacks inherent in arc ignition are the relatively poor energy transfer to the fluid as well as the significant erosion of the electrode material.

The HAN-based propellants such as LGP 1846 are good conductors. The conductivity of LGP 1846 is $\kappa = 0.08 \text{ cm}^{-1}\Omega^{-1}$ at room temperature, which corresponds to that of a 0.73 molar KCl solution. The high salt content of LGP 1846 makes it behave more like a molten salt than an aqueous solution [9]. On application of a voltage pulse, electric current is conducted through the propellant due to ion migration. The concomitant ohmic heating and chemical chain reactions of propellant components culminate in self-sustained combustion.

1.2.1 Electrical Ignition

In the earlier work on electrical ignition of HAN-based liquid propellants the emphasis was on ignition by high current arcs. Indeed, a functioning igniter system for a 155-mm RLPG has been demonstrated [5]. Nevertheless, it was realized that a major part of the total energy transfer to the liquid propellant takes place before breakdown occurs. Irish [10] attributed the energy transfer

to ohmic heating of the liquid propellant during this so-called "formative" phase. The mathematical model was based on the electrode geometry shown in Figure 2.

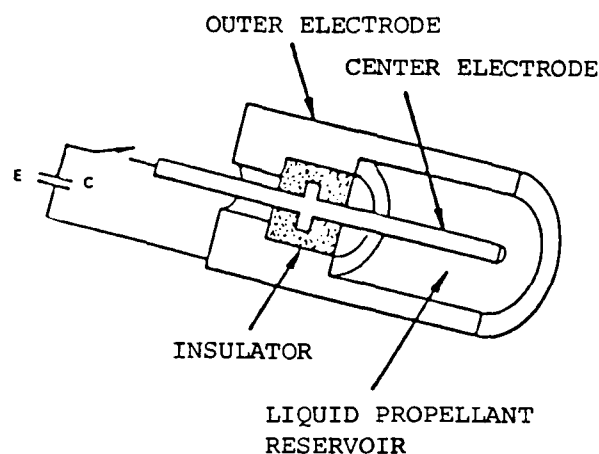


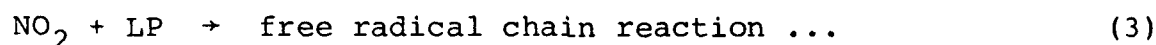
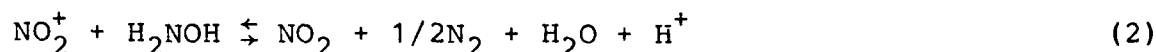
Fig. 2. Basic electrode geometry (Naval Ordnance Station, Indian Head, USA [10]).

According to the model [10], heating of the liquid propellant originates at the locus of highest field and ion flux densities, i.e., along the inner electrode, and is continuously transmitted outward through concentric "shells" of the liquid. Once the boiling point of the liquid is reached, a vapor sheath is formed at the inner electrode, which then assists in arc formation. The model was satisfactory in calculating the energy transfer during the "ohmic" portion of the formative phase, but did not predict total energy consumption. Deviation from experiment was up to 45%. Moreover, the grid spacing had to be iterated empirically.

Other experiments have definitely shown that, in addition to ohmic heating, electrolytical or electrochemical processes are also relevant to the electrical ignition of HAN-based propellants. Carleton et al. [11] were able to demonstrate that NO_2 develops at the anode followed by heat generated emission of light from the same electrode. No arc was generated during these experiments. Furthermore, the arrangement of the electrodes was such, that the simple model of Irish [10] would have predicted equal heating rates at both electrodes.

Thermal decomposition studies [12-14] have shown that the oxidizer component, HAN, reacts first, decomposing into reactive intermediates, among them NO_2^+ , NO_2 , and NO . The importance of NO_2 and NO as reaction intermediates have been recognized through isotopic tracer studies [13]. It comes as a surprise that the HAN has reacted almost completely during the early pressure rise in the closed reaction vessel. The fuel component seems to play no important part in the ignition. It does, however, determine the total energy content of the liquid propellant [15].

According to N. Klein and coworkers [12], NO_2^+ initiates the decomposition of HAN. On applying an electric field to a HAN containing solution, i.e., LGP 1846, the nitrate ions migrate to the anode. Nitronium ions are formed when the increasing nitrate ion concentration in the vicinity of the anode shifts the chemical equilibrium (1) to the right. The nitronium ions then initiate the reaction sequences leading to combustion.



Presence of nitronium ion alone, however, is not sufficient in effecting self-sustained combustion [16]. The liquid propellant will need a certain degree of confinement to allow pressure buildup [15] and also heating for the decomposition reactions to go over into self-sustained combustion.

1.2.2 Computer Aided Igniter Design

The theoretical assumptions behind the numerical igniter design optimization studies for arcless igniters are shared with Irish [10] insofar as the evolution of heat and the rates of chemical processes in a strongly divergent electric field will be selectively accelerated in areas of high field density. As is well known, the electric field lines correspond to lines of constant current. Given that the principal reaction chemistry of ignition takes place at only one electrode, for example, the anode [11], an optimized electrode geometry should facilitate ignition at this electrode. In a basic concentric design as encountered in the igniter types studied herein it should be preferable to ensure that ignition takes place exclusively at a defined location; for instance, at the tip of the center electrode. An immediate consequence, needing no calculation, would be to make the center electrode act as anode. The optimal electrode shapes would then be found by numerical procedures.

Figure 3 illustrates this point. Representative field lines as well as equipotential lines are shown for the BRL(m/l) configuration. Visibly, the highest density of field lines is near the center electrode tip; a second less pronounced density maximum is located at the edge of the outer electrode. Later we shall see that an optimized igniter needs tailoring of the field line density on both electrodes.

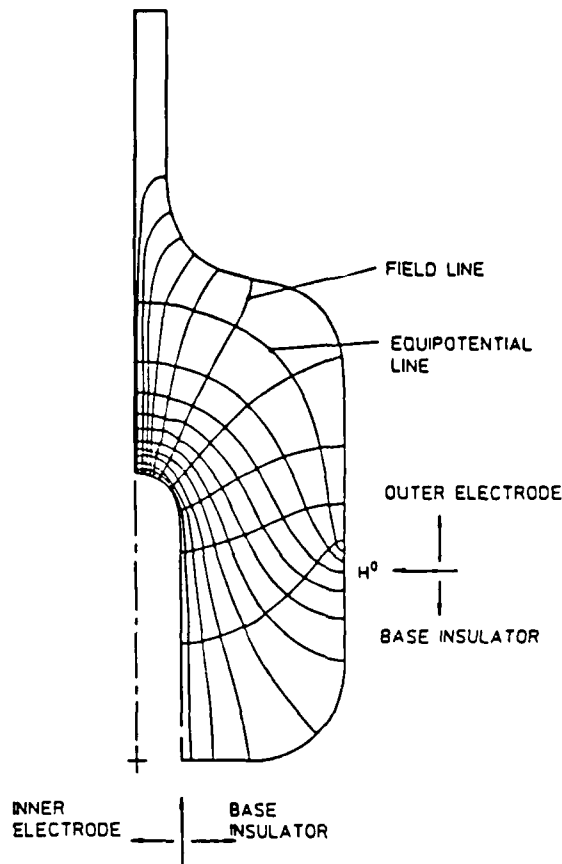


Fig. 3. Calculated electric field lines and equipotential surfaces for igniter configuration BRL(m/l).

2. EXPERIMENTAL

2.1 EMI-AFB Ignition Test Fixture 1

Initially, tests were conducted with a replica of the BRL ignition test fixture shown in Figure 4. The apparatus consists of the electrode mount assembly in the lower half of Figure 4 and the housing in the upper half. The chamber volume may be varied between 60 and 100 cm³, an opening at the side holds the rupture disk. A Kistler pressure gauge was mounted at the top of the housing directly across from the igniter vent orifice as shown. As a side effect, the hot, partially combusted efflux from the vent orifice of the igniter was also registered by the gauge.

A modified chamber was built as shown in Figure 5 with the opening for the pressure gauge no longer pointing at the vent but perpendicular to the axis of the effluent flow. Two of the total of three inserts are shown. The additional port enables simultaneous optical measurements via temperature gauges or sapphire windows.

TEST FIXTURE
ELECTRICAL IGNITION OF HAN-BASED LP

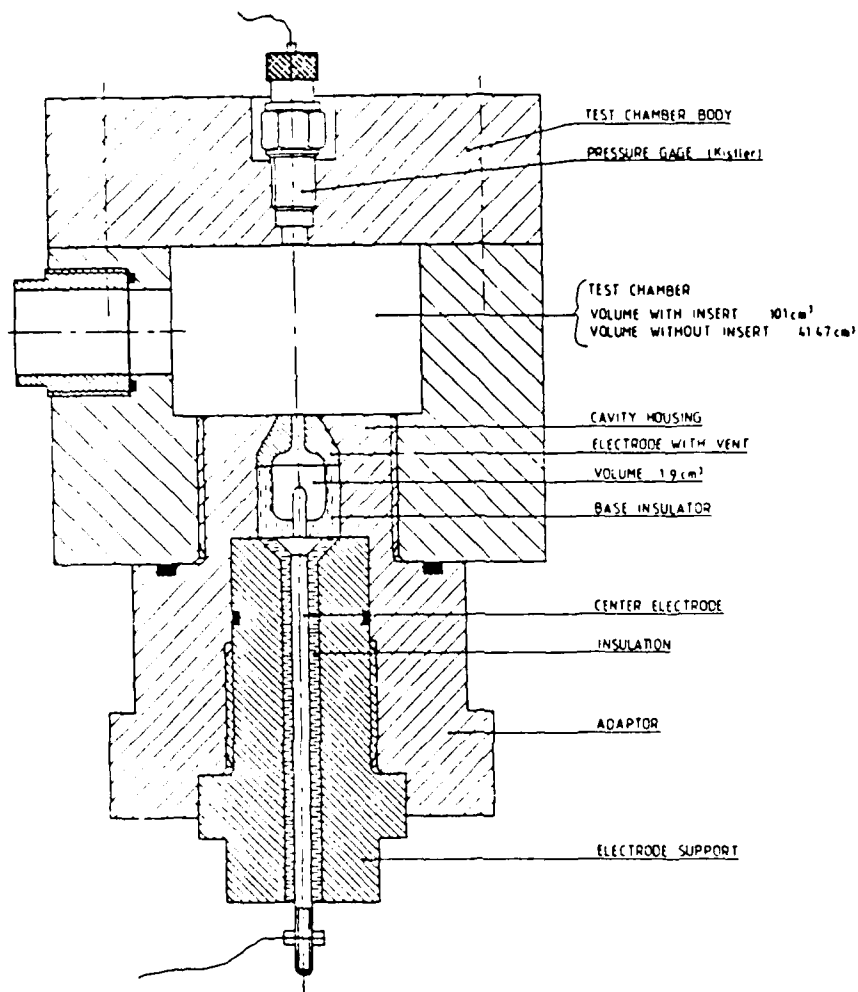


Fig. 4. EMI-AFB ignition test fixture 1.

Moreover, the pressure gauge is electrically insulated from the chamber walls. The rupture disk placed in the remaining port serves as a safety valve.

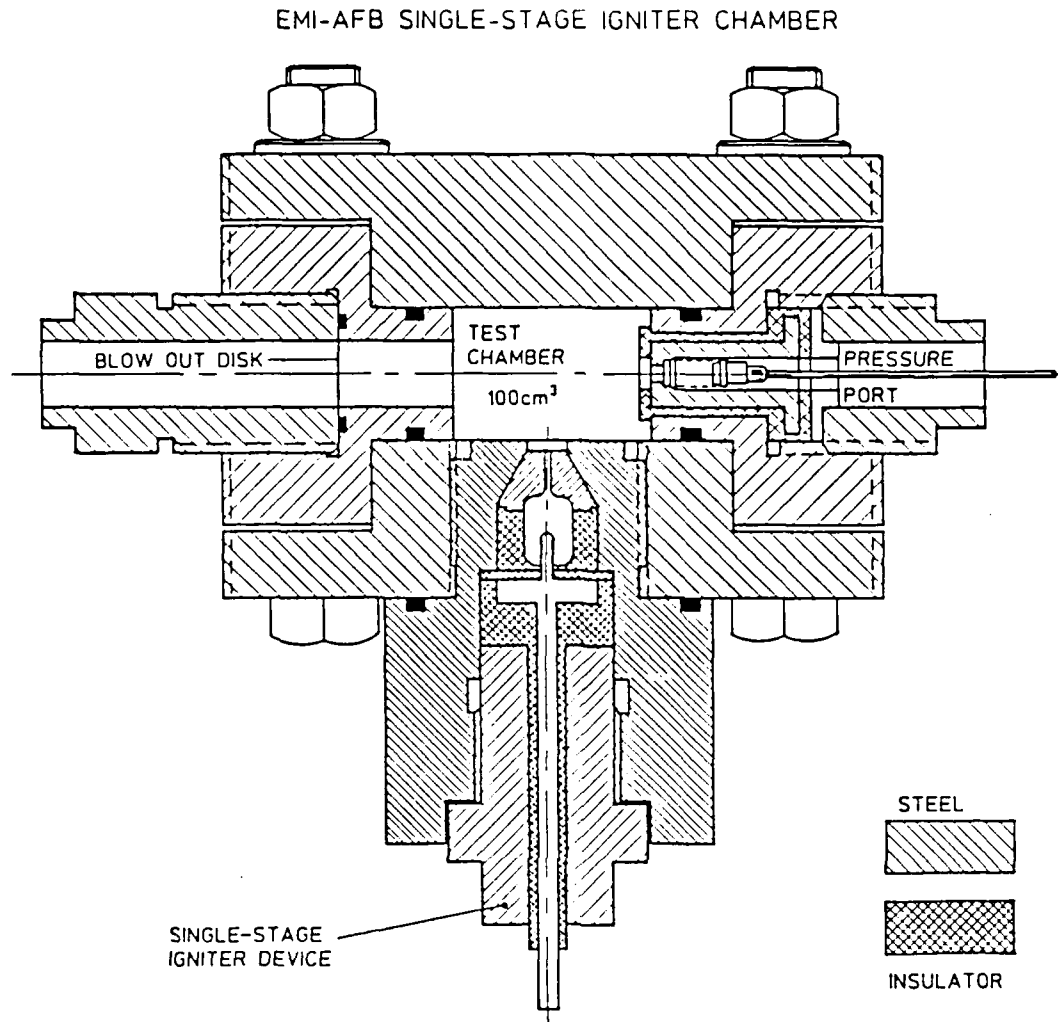


Fig. 5. Modified EMI-AFB ignition test fixture with electrically insulated pressure transducers.

2.1.1 Igniter Mount Assembly

A total of six different igniter electrode geometries, i.e., configurations, were employed. These were mounted interchangeably in the assembly shown in Figure 6. Figures 7 and 8 show in detail the electrode holder and adapter both made of steel. The different igniter geometries show some overall similarities. The basic design features are shown in Figure 9 for the original BRL type igniter cavities. These are roughly described by their inner and outer electrode sizes, namely: l, m, s or large, medium, and small. The center electrode is denoted first followed by the outer electrode. For example, "(m/s)" signifies a medium center (inner) electrode and a small outer electrode.

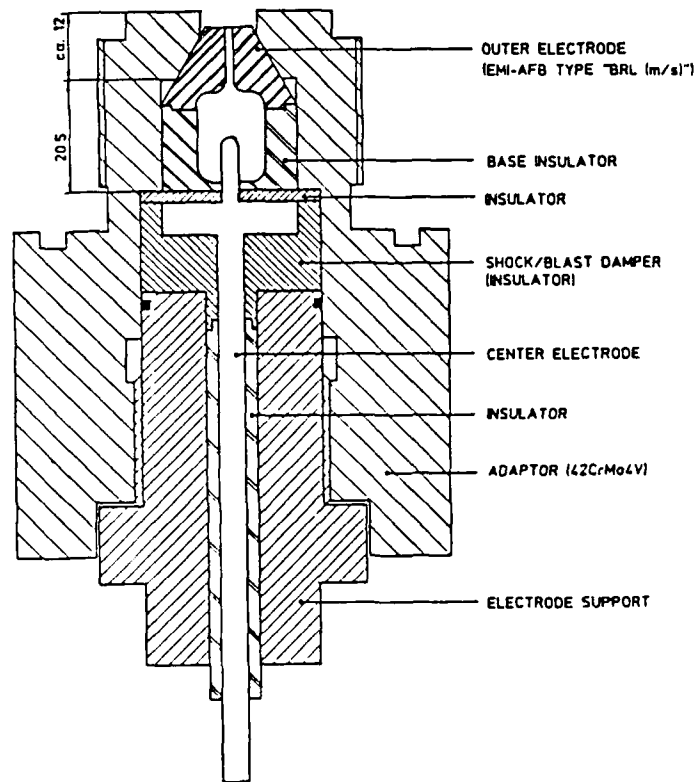


Fig. 6. EMI-AFB electrode support with the "BRL(m/s)" type igniter.

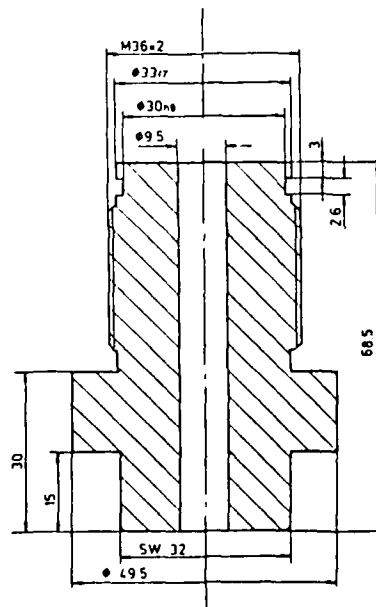


Fig. 7. Electrode holder.

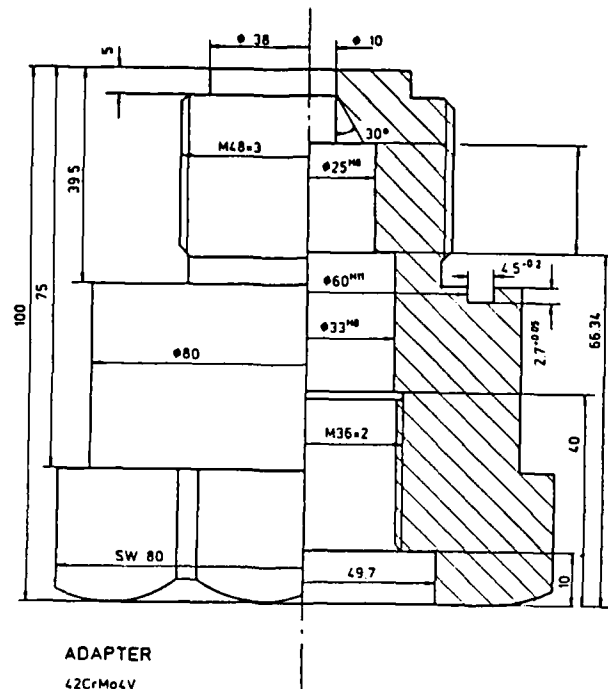


Fig. 8. Adapter for placement of electrode holder in housing.

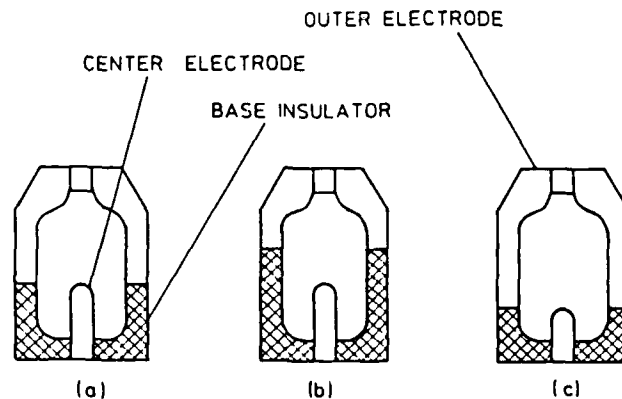


Fig. 9. Basic BRL igniter cavity configurations: (a) (m/m); (b) (m/s); (c) (s/l).

In the tests described herein the inner electrode has essentially the same overall dimensions as shown in Figure 10. The sole parameter varied was the in-chamber electrode length, l_I . A special steel, RemanitTM 1.4401, was used for improved corrosion resistance. The electrode surface was always smoothed with SiC-sandpaper of particle density 1000 (DIN) prior to each test except for the DNAG-EMI-AFB-5 type igniter which is described further below.

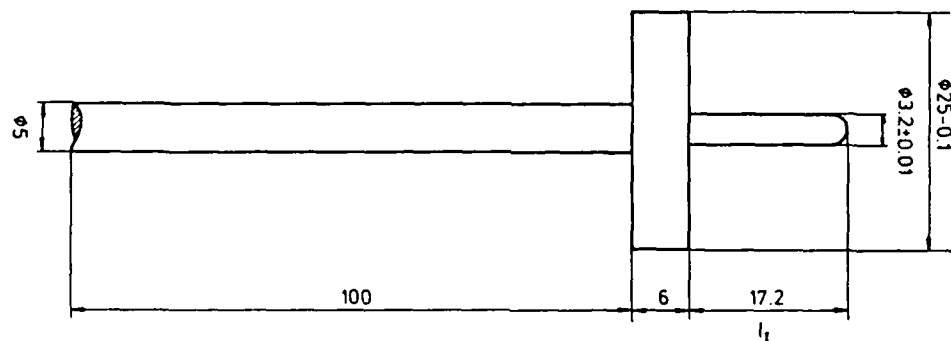


Fig. 10. Center electrode type I; in-cavity immersion length: l_I ; material: Remanit 1.4401.

The outer electrode is separated from the inner electrode by the base insulator of shock resistant plastic (polyoxymethylene copolymer: SustarinTM, Hoechst), which also acts as a shock damping cavity wall. The outer electrode and base insulator for the EMI-AFB type "BRL(m/s)" configuration are drawn schematically in Figure 11.

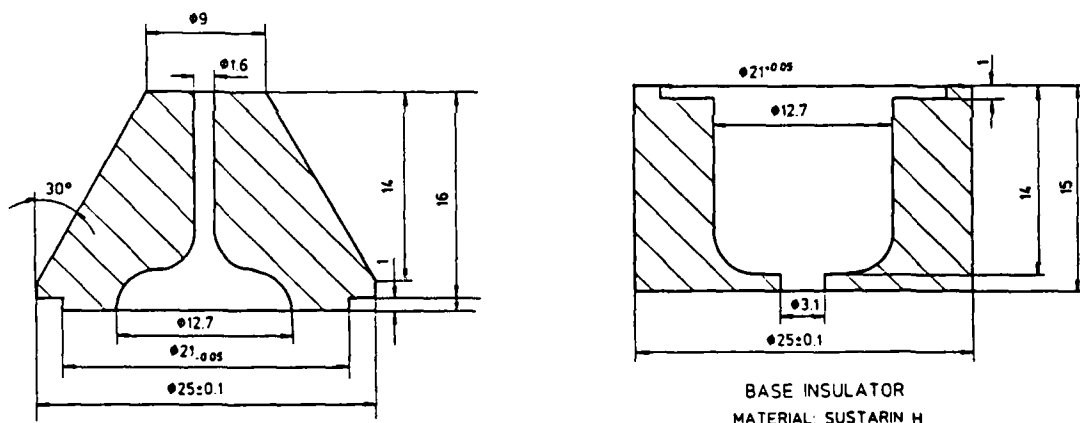


Fig. 11. Outer electrode and base insulator (insulator no. 1) for the electrode configuration EMI-AFB type "BRL(m/s)".

In addition, the inner electrode is also separated from the electrode holder by a sheath of insulating material (SustarinTM), which is enlarged into a shock absorbing "collar" at the top. The complete assembly, except for the electrode holder, is shown in Figure 12.

IGNITER: EMI-AFB TYP "BRL (m/s)"
(CENTER ELECTRODE TYPE I)

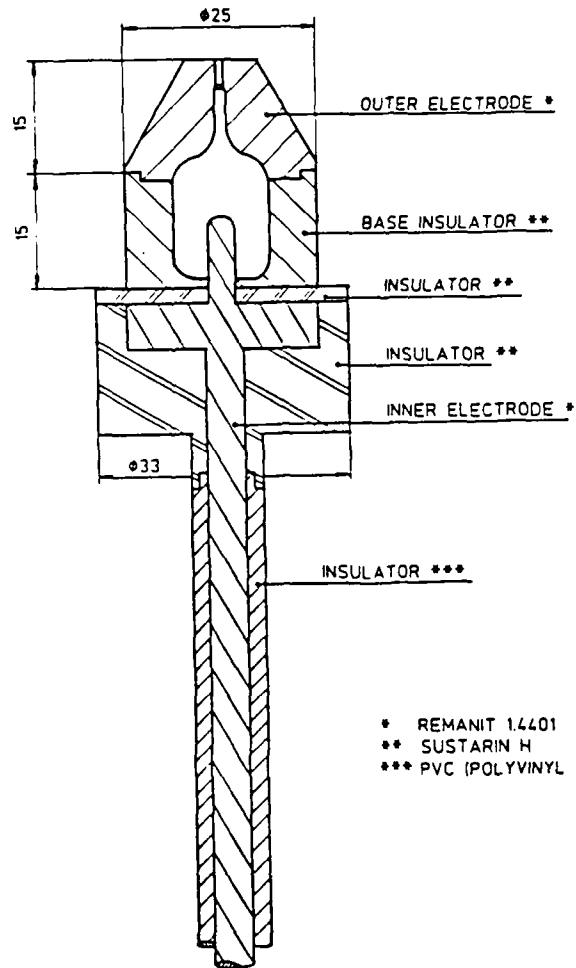


Fig. 12. Assembled electrode configuration EMI-AFB type "BRL (m/s)".

2.1.2 Electrode Configurations

The construction principles and dimensions of the six different electrode configurations are summarized in Tables 1 and 2.

Table 1. Electrode configurations tested with EMI-AFB ignition test fixture 1

Cavity Types	Inner Electrode Length l_I [mm]	Outer Electrode Shape Sections from Top				Surface
		1	2	3	4	
EMI-BRL (m/s)	8.1	90° hs; # $r = 3$ mm concave	180° hs; $r = 3$ mm convex	-	-	*
EMI-AFB - 1	5.6	"	180° hs; $r = 8$ mm convex	-	-	*
EMI-AFB - 2	12.6	"	180° hs; $r = 6.5$ mm convex	-	-	*
EMI-AFB - 3	4.6	"	40° hs; $r = 8$ mm convex	60° cone	-	*
EMI-AFB - 4a	8.2	40° hs; $r = 3$ mm concave	45° cone	36° cone	18° cone	*
EMI-AFB - 4b	5.2	"	"	"	"	*
DNAG-EMI-AFB-5a	8.23	54° hs; $r = 3$ mm concave	paraboloid	21° hs; $r = 3$ mm convex	"	coarse
DNAG-EMI-AFB-5b	8.23	"	"	"		medium
DNAG-EMI-AFB-5c	8.23	"	"	"		fine
Surface Roughness	R_a [μ m]	R_z [μ m]	R_{max} [μ m]			
coarse	0.67	3.74	4.64			
medium	0.37	2.26	2.26			
fine	0.16	1.28	1.38			

* \approx DIN 1000 grade sandpaper

\approx hs: hollow sphere

R_a : average distance between surface protrusions

R_z : average height of protrusions

R_{max} : maximum R_z

Table 2. Electrode surface areas

Electrode Configu- ration	Inner Electrode Length l_I [mm]	Inner Electrode Area A_{Si} [mm ²]	Outer Electrode Area A_{So} [mm ²]	Area Ratio Q A_{Si}/A_{So} [mm ²]
EMI-AFB/BRL (m/s)	8.1	81.4	198.3	0.41
EMI-AFB - 1	5.6	56.3	400.0	0.141
EMI-AFB - 2	12.1	126.7	263.5	0.481
EMI-AFB - 3	4.6	46.3	442.5	0.105
EMI-AFB - 3-SG	4.6	46.3	442.5	0.105
EMI-AFB - 4a	8.2	82.4	602.0	0.137
EMI-AFB - 4b	5.2	52.3	602.0	0.087
DNAG-EMI-AFB-5a	8.23	82.7	506.8	0.163
DNAG-EMI-AFB-5b	8.23	82.7	506.8	0.163
DNAG-EMI-AFB-5c	8.23	82.7	506.8	0.163

2.1.2.1 EMI-AFB Type "BRL(m/s)"

As mentioned previously, the first tests were conducted with a replica of the BRL(m/s) configuration. Details of the outer electrode and base insulator are given in Figure 13. The inner electrode length, l_I , is 8.1 mm, which gives a surface area of the inner electrode, $A_{Si} = 81.4 \text{ mm}^2$. The outer electrode surface area is $A_{So} = 198.3 \text{ mm}^2$. The resulting cavity is cylindrical in shape.

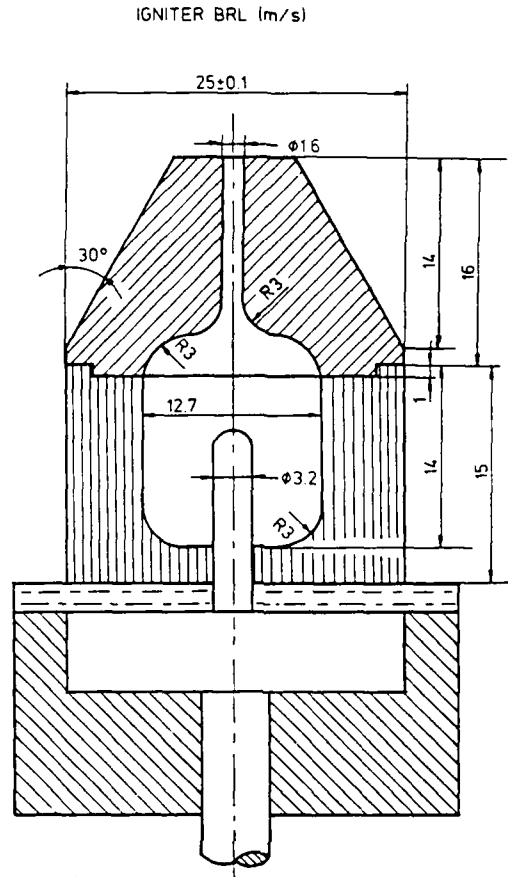


Fig. 13. Electrode configuration BRL(m/s).

2.1.2.2 Configurations EMI-AFB-1 and EMI-AFB-2

Detailed schematic drawings of the elementary configurations EMI-AFB-1 and EMI-AFB-2 are depicted in Figures 14 and 15, respectively.

The geometries of the configurations EMI-AFB-1 and EMI-AFB-2 differ from each other in three respects. First, the distance from the cavity bottom to the upper rim of the base insulator is 4 and 11 mm, respectively. Second, because the same inner electrode was used in both cases, the effective inner electrode lengths, l_I , are 5.6 and 12.6 mm, respectively. Third, the geometry of configuration EMI-AFB-1 is close to that of a half-sphere ($r = 8$ mm) as opposed to the rather elongated, spherically topped ($r = 6.5$ mm), cylindrical shape of configuration EMI-AFB-2. The latter geometry is even more elongated than that of the EMI-AFB type "BRL(m/s)".

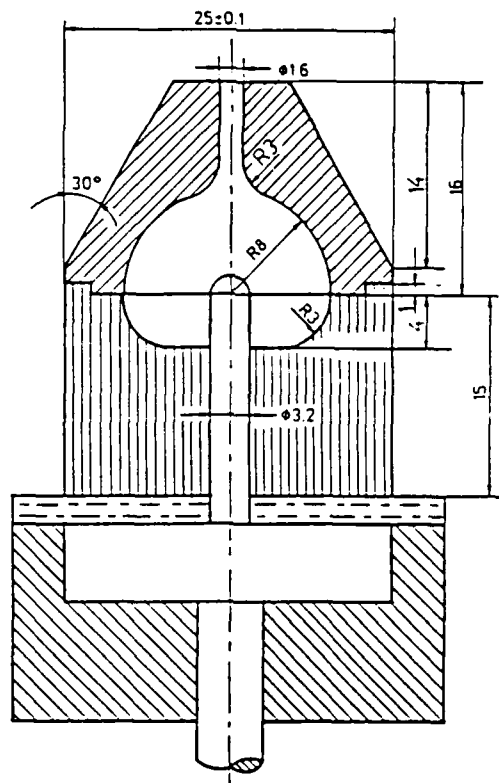


Fig. 14. Electrode configuration EMI-AFB-1.

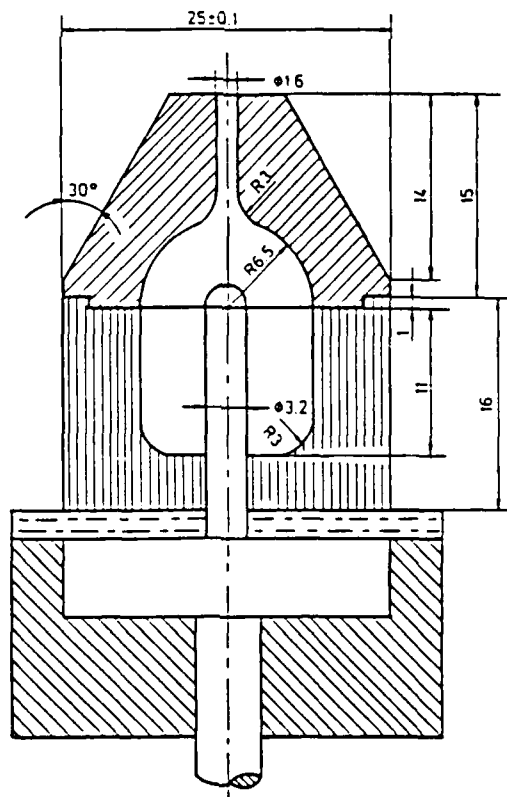


Fig. 15. Electrode configuration EMI-AFB-2.

2.1.2.3 Configurations EMI-AFB-3 and EMI-AFB-4

The electrode configuration EMI-AFB-3 is shown in Figure 16. The cavity geometry is characterized by a spherical upper section ($r = 8$ mm) and a 60° conical flank. The inner electrode length is $l_I = 4.6$ mm. With this geometry the amount of propellant near the cavity base is increased compared to cylindrical or spherical shapes. Accordingly, there is less self-confinement of the propellant between the two electrodes.

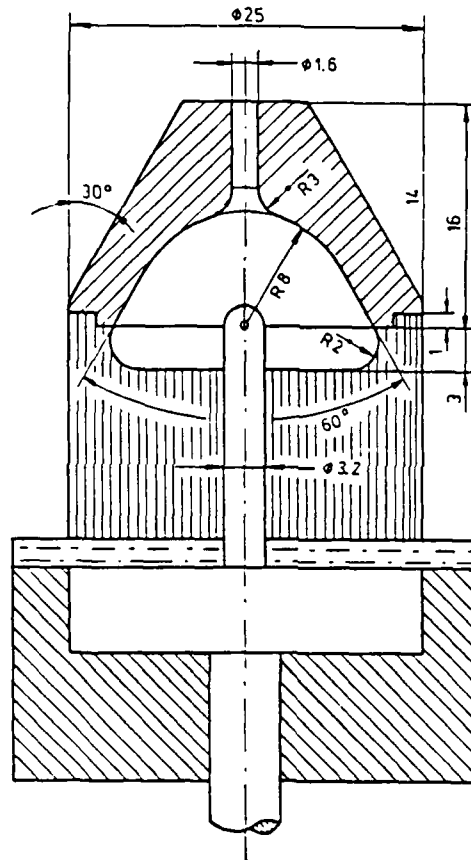


Fig. 16. Electrode configuration EMI-AFB-3.

The igniter EMI-AFB-4 has a more complicated design as shown in Figure 17. The lower part of the outer electrode consists of not one but three conical sections. Two different inner electrode lengths, l_I , of 8.2 and 5.2 mm were denoted 4a and 4b, respectively. The geometry approximates the parabolic contour of the configuration DNAG-EMI-AFB-5 (described below) by straight conical sections.

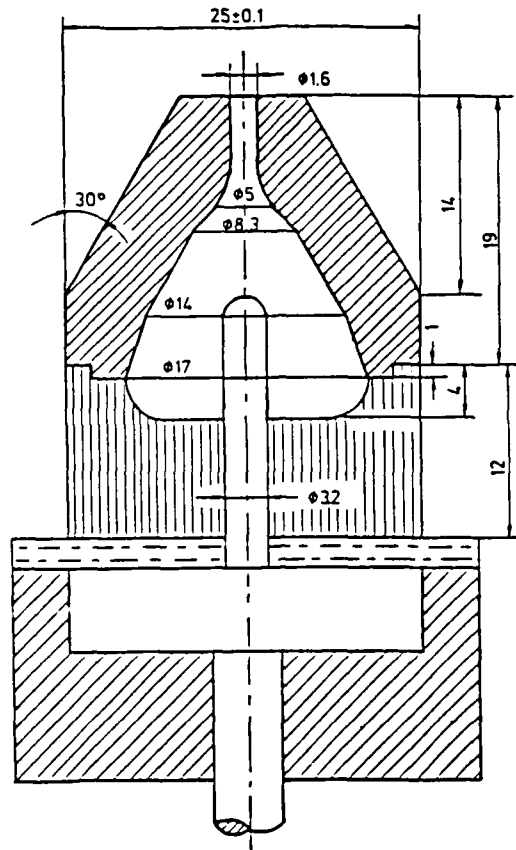


Fig. 17. Electrode configuration EMI-AFB-4a.

2.1.2.4 Configuration DNAG-EMI-AFB-5

As described in Section 3.1.5, numerical calculations carried out at Dynamit Nobel AG (DNAG) indicated that, other parameters remaining equal, a parabolic contour of the outer electrode constitutes an optimized electrical field or current flow line geometry, that should result in an improved igniter performance. One such parabolic geometry is realized in the electrode configuration DNAG-EMI-AFB-5 shown schematically in Figure 18 and as an assembly in Figure 19.

The igniter DNAG-EMI-AFB-5 was built in three versions with different surface roughnesses. Treatment of the electrode surfaces by an electro-erosion process afforded the desired well-defined surface qualities according to DIN 4768. This work was done by DNAG. The resultant "finishes" are described by a set of three characteristic lengths or radii (see Table 1): R_a = average crest to crest distance between surface protrusions, R_z = average height of protrusions, and R_{max} = maximum R_z .

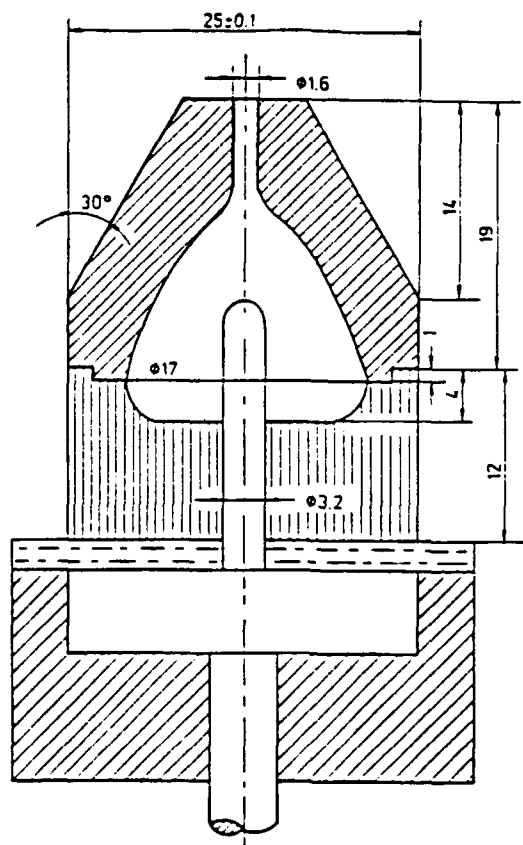


Fig. 18. Electrode configuration DNAG-EMI-AFB-5.

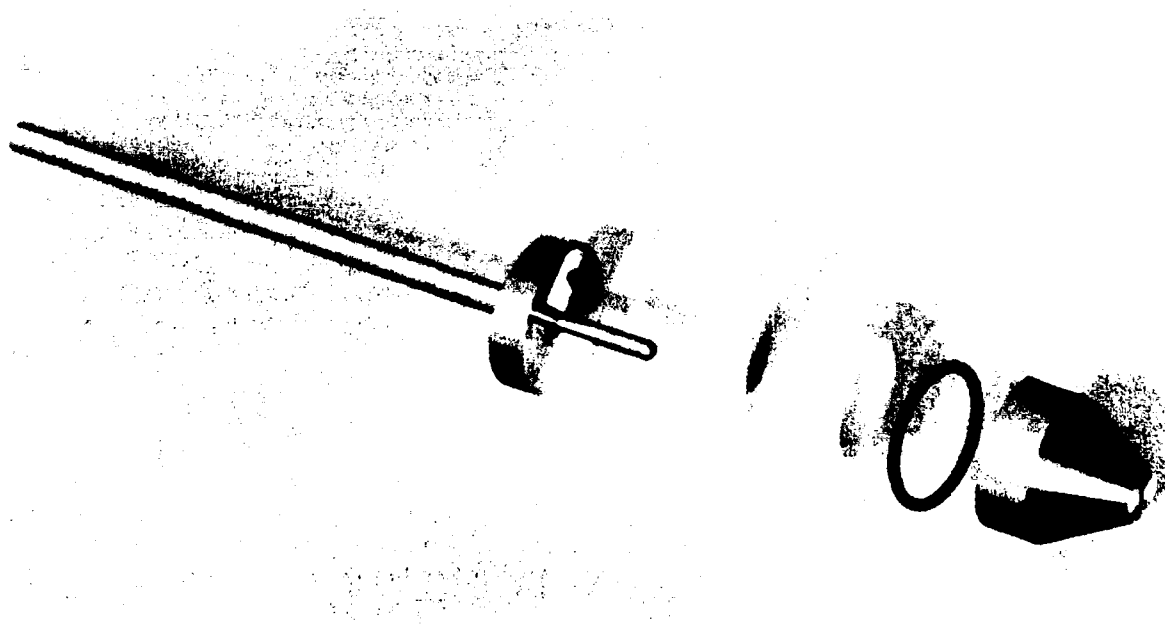


Fig. 19. Assembled electrode configuration DNAG-EMI-AFB-5.

2.2 EMI-AFB Ignition Test Fixture 2

The test fixture shown in Figure 20 was built for basic ignition studies. The fixture is equipped with sapphire windows (Figure 21). The ignition events were in many cases monitored by a high speed HYCAM photographic recording on black and white daylight film in both the emission and transmission modes with a frame speed of 4 kHz. Various electrode configurations are shown in Figure 22. The liquid propellant volume ranged from 3 to 7 cm³ via teflon inserts.

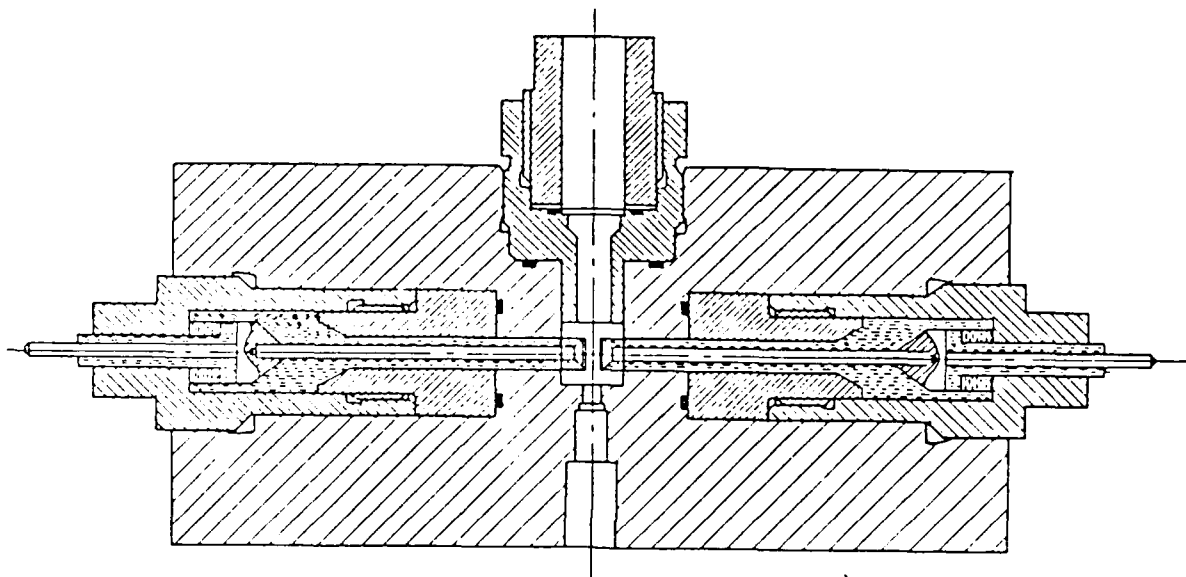


Fig. 20. EMI-AFB ignition test fixture 2.

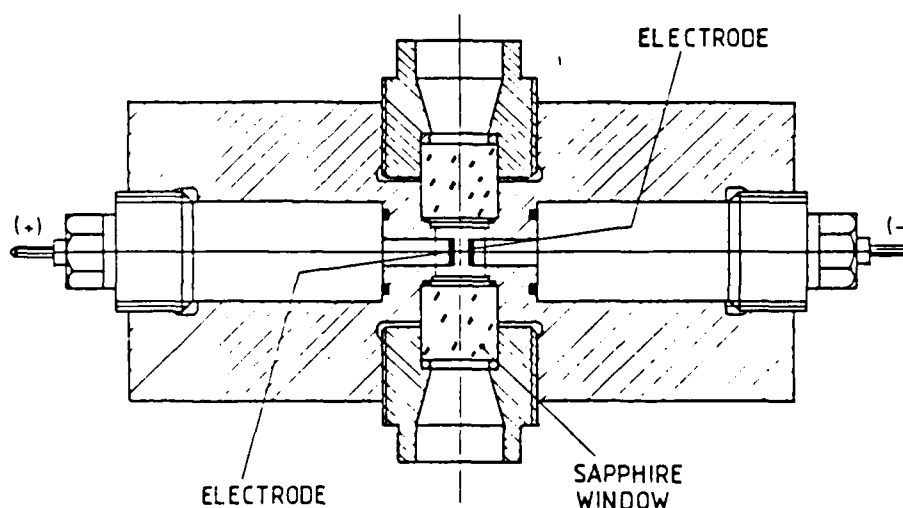


Fig. 21. Position of sapphire windows in EMI-AFB test fixture 2.

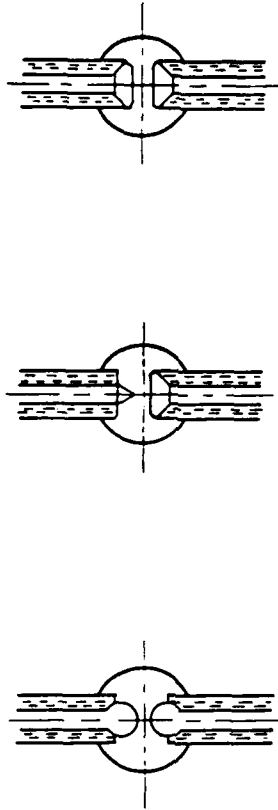


Fig. 22. Electrode configurations for EMI-AFB test fixture 2.

2.3 Electrical Power Supply

The supply circuit used for the tests is shown schematically in Figure 23. A constant voltage (1500 - 1800 V) was applied to the igniter electrodes via capacitors with 200 μ F capacity. An inductor having an inductance of 28 mH and a resistance of 1.1 ohm was included in the circuit. The main contribution to the resistance was by the LGP 1846 itself, measuring roughly 50 ohm (EMI-AFB-3) against a small (1 V) DC current. The medium rise time of the voltage step was approximately 0.6 to 0.8 ms. The closing of the supply circuit triggered the diagnostics.

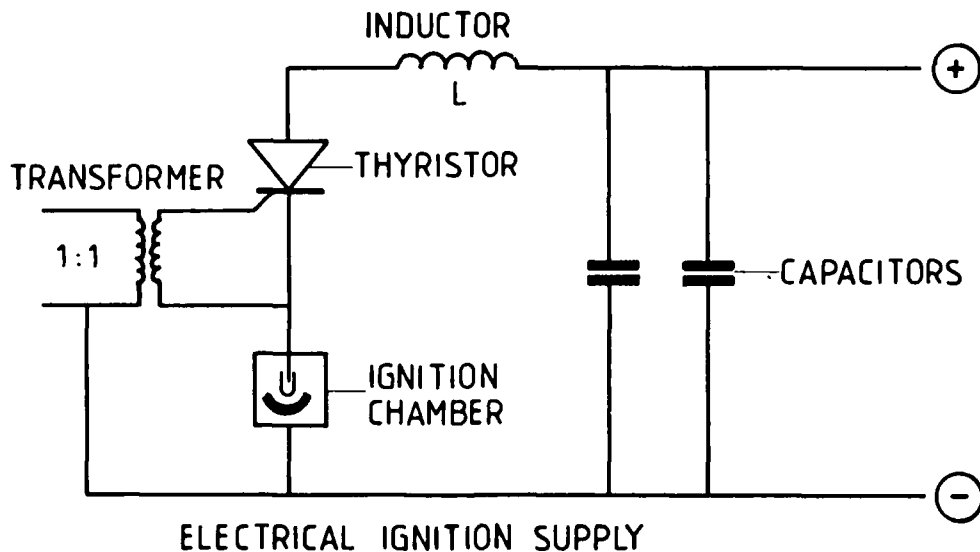


Fig. 23. Electric ignition power supply circuit.

2.4 Numerical Calculations

Computer aided design of igniter configurations may help in avoiding excessive experimental trial and error. As a first step in this direction the electrostatic field and equipotential line distributions were calculated at DNAG. DNAG supported this contract work in accord with the German Ministry of Defense.

A finite element code program, SYSTUS, was used for the computations [17] on a VAX computer. Owing to the rotational symmetry of the systems under study only right side half-cavities needed to be evaluated. Figure 3 shows the result of such a calculation. The boundary between the outer electrode and the base insulator is marked by H^0 .

2.5 30-mm RLPG Simulator

The EMI-AFB 30-mm RLPG simulator is described elsewhere [18]. Its combustion chamber is 20 cm^3 in volume. The injection principle is of the simple showerhead type. The injector faces are studded with 24 orifices of various diameters. Figure 24 shows a schematic of the adaptor for the single-stage igniters described above. As is readily confirmed from the drawing, the outer contour of the single-stage igniter fits into the adaptor. The long neck of the adaptor, which connects it to the RLPG simulator combustion chamber, had an inner diameter of 4.5 mm.

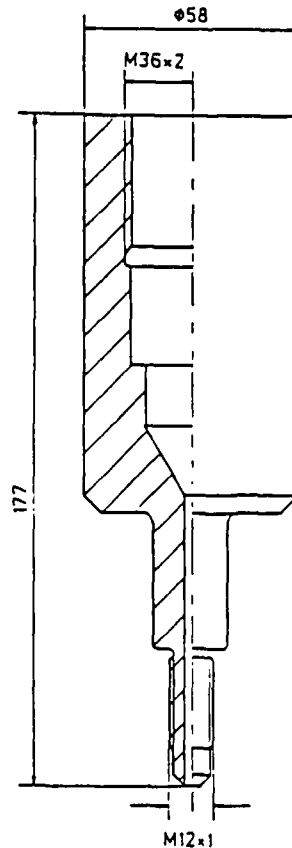


Fig. 24. Schematic of igniter adapter to 30-mm RLPG.

The injection geometry of the 30-mm RLPG simulator causes destructive pressure fluctuations when the injector is not optimized and the liquid propellant reservoir is filled with an energetic liquid propellant such as LGP 1846. Instead, nitromethane-methanol (NM) 80/20 w/w was chosen since it is less energetic. Of course, the igniter itself was filled with LGP 1846, which, contrary to non-modified NM 80/20, is a conductor.

The igniter position when mounted next to the simulator is no longer vertical, as in the EMI-AFB test fixture 1, but horizontal. To prevent leakage of the liquid propellant in this position, the vent orifice was sealed with silicon grease in the first tests. From test No. 8 on a plastic foil of 0.018 mm thickness was glued over the opening. Electrical ignition was successful and is now being used routinely in normal test operation of the 30-mm RLPG simulator.

2.6 IR Spectroscopy

A 96-channel infrared spectroradiometer was employed for measurements of the IR emissions from liquid propellant combustion during the 30-mm RLPG test firings. The spectrometer is constructed so that the incoming light falls on two separate entrance openings and from there travels through two symmetrically arranged sets of optics. Two low pass filters behind the entrance sort the light into two paths defined by the cut on frequencies of 1.4 and 2.6 μm . Optical dispersion is achieved by gratings spanning about one octave each in frequency. The diffracted light is incident on two separate, linear, 48 element detector arrays.

The total spectral range lies between 0.64 and 2.67 μm for the short wavelength portion, which is narrowed by the entrance filter to 1.4 to 2.67 μm and 2.4 and 5.32 μm for the long wavelengths. The temporal resolution for digital collection of full spectra is 12.5 ms with chopper and 1 ms without. Operation as a 96-channel analogue spectrometer is also possible. In this mode the digital data logging is nonfunctional. The channels are accessible via BNC cable. Time resolution is again 1 ms per spectrum.

The instrument is calibrated against a 1000 K blackbody and the deviation of the experimental intensity from the internally stored Planck function expressed as a coefficient matrix:

$$E \cdot S^{-1} = C .$$

The ratio of the expected signal, E, over the measured signal, S, is stored as the calibration factor channel by channel, C. The result is a 96-value calibration matrix. A 1000 K blackbody exhibits a theoretical spectral radiant exitance of:

$$M(\lambda, T) = 1.286 \cdot 10^4 \text{ [W/m}^2\text{ }\mu\text{m]} \quad \lambda = 2.92 \text{ }\mu\text{m} .$$

The signal output that corresponds to a 1000 K source is 1.286 volt after calibration. Detector noise is ± 0.02 % of the total range.

3. RESULTS

The parameters in our experiments with LGP 1846 were chosen in such a way as to avoid unwanted arc ignition. Only arcless "electrochemical" or "soft" ignition was of interest. Indeed, when arcing actually did occur, substantial electrode pitting was invariably the result. Note that the steel chosen as less corrosive electrode material, Remanit 1.4401, was relatively soft. Consequently, changes of the electrode surface including material fatigue are more easily detected.

The igniter designs tested are also suited, in principle, for the study of arc ignition of non-conducting liquid propellants such as the nitromethane/methanol mixtures. This would necessitate higher field strengths than those currently in use. Alternatively, it is possible to add organic salts, in order to raise the conductivity of these mixtures and thus achieve arcless or electrochemical ignition [19].

3.1 EMI-AFB Ignition Test Fixture 1

A total of six different igniter configurations were tested. The shapes of the outer electrode and the base insulator are the main factors in determining the cavity geometry and thus the distribution of liquid propellant in the cavity. The inner electrodes had the same shape throughout all tests and were varied only in length, l_I . The igniter configurations fall into four categories:

- Spherical : EMI-AFB-1
- Cylindrical : BRL(m/s); EMI-AFB-2
- Conical : EMI-AFB-3
- Paraboloid : EMI-AFB-4, DNAG-EMI-AFB-5

The EMI-AFB-4 type is an approximation to the paraboloid shape obtained by numerical calculation.

The following parameters were varied:

- test chamber relaxation volume (60 cm^3 and 100 cm^3),
- confinement of the liquid propellant charge, i.e., vent diameter (1.4 to 2.0 mm),
- electrode polarity (either positive or negative),
- electrode surface areas,
- electrode length, l_I ,
- distribution of the liquid propellant (LP) mass in the reservoir.

The test results are summarized in Table 3 and have been grouped into sets to facilitate viewing of the data. Included are the maximum or integral values of the electrical parameters recorded:

- Voltage I_{\max} (A)
- Current U_{\max} (V)

- Power P_{\max} (kW)
- Energy E_{\max} (J)

Also presented in the table are:

- Charge voltage, U_L (V),
- Ignition delay time, $t_{10\%}$ or t_2 (ms); measured at 10% of maximum pressure,
- Rise time, $t_{90\%} - t_{10\%}$ (ms); measured at 10% to 90% of maximum pressure,
- Maximum chamber pressure, p_{\max} (MPa).

The maximum values in the table were taken from the appropriate time plots obtained experimentally. The maximum pressure is, of course, meaningful only in the closed bomb mode. A burst disk was used throughout test sets 1 and 4, except test 48 (set 4). It was also used in test 156 (set 11).

Table 3. Results of test firings

Test Set	Test No.	Vent Orifice Diam. [mm]	U_L [V]	U_{max} [V]	I_{max} [A]	P_{max} [kW]	E_{max} [I]	$t_{10\%}$ [ms]	$t_{90-10\%}$ [ms]	P_{max} [MPa]
1	<u>EMI-AFB Type "BRL(m/s)"; chamber volume 60 cm³; positive center electrode</u>									
	28	1.8	1750	1600	128	184	101	3.0	0.8	16.5 ^b
	29	1.8	1750	1620	127	184	94	2.9	0.9	16.0 ^b
	30	1.8	1750	1660	130	193	91	3.0	0.9	15.9 ^b
	31	1.6	1750	1700	132	192	79	1.65	0.6	16.4 ^b
	32	1.6	1850	1660	147	193	88	1.75	0.95	15.1 ^b
2	<u>EMI-AFB Type "BRL(m/s)"; chamber volume 100 cm³; positive center electrode</u>									
	54	1.6	1750	1560	140	200	85	2.1	5.6	9.0
	57	1.6	1750	1650	130	194	63	1.7	4.3	12.0
	58	1.6	1750	1580	145	208	78	3.0	5.7	12.5
	59	1.6	1750	1650	133	195	60	2.2	6.1	8.5
	61	1.6	1750	1560	153	210	84	2.5	3.8	9.5
	62 ^{ac}	1.6	1750	1560	153	215	83	2.7	4.8	7.5
3	<u>EMI-AFB Type "BRL(m/s)"; chamber volume 100 cm³; negative center electrode</u>									
	193 ^c	1.6	1560	990	156	154	175	2.9	1.6	4.5
	195 ^a	1.6	1560	1050	148	155	186	4.05	2.55	3.5
	196 ^c	1.6	1520	1140	147	165	170	4.5	3.2	15.6
	197 ^a	1.6	1520	1150	144	160	134	3.9	2.2	6.4
	198 ^c	1.6	1520	1180	140	159	140	3.9	1.8	2.9
4	<u>EMI-AFB - 1; chamber volume 60 cm³; positive center electrode</u>									
	35 ^d	2.0	1650	1510	183	226	63	--	--	--
	38	1.6	1650	1490	180	215	66	1.35	1.05	11.6 ^b
	39	1.8	1650	1550	178	222	62	1.35	1.1	12.0 ^b
	42	2.0	1650	1560	170	210	56	1.2	0.9	12.5 ^b
	44	2.0	1750	1700	182	247	59	1.0	1.0	11.3 ^b
	48	1.8	1750	1700	180	255	53	1.2	2.2	22.0
	49	1.8	1750	1700	170	235	58	2.4	1.8	12.3 ^b

a: Incomplete combustion; b: Rupture disk limits P_{max} ; c: Materials failure;
d: No ignition

Table 3. Results of test firings (continued)

Test Set	Test No.	Vent Orifice Diam. [mm]	U_L [V]	U_{max} [V]	I_{max} [A]	P_{max} [kW]	E_{max} [I]	$t_{10\%}$ [ms]	$t_{90-10\%}$ [ms]	P_{max} [MPa]
5	<u>EMI-AFB - 1; chamber volume 100 cm³; positive center electrode</u>									
	52	1.6	1750	1680	175	245	65	3.0	3.8	13.4
	63 ^a	1.6	1750	1640	175	240	60	2.9	2.4	9.7
	65 ^c	1.6	1750	1650	180	240	64	2.9	4.6	8.5
	66	1.6	1750	1600	190	248	69	1.2	3.9	11.5
	67 ^a	1.6	1750	1670	180	248	59	3.5	6.2	8.5
6	<u>EMI-AFB - 1; chamber volume 100 cm³; negative center electrode</u>									
	182 ^c	1.6	1610	1280	195	214	107	4.05	1.45	7.0
	184	1.6	1610	1260	193	208	106	3.8	2.4	4.9
	185 ^c	1.6	1610	1300	192	210	99	2.5	1.3	4.6
	186 ^c	1.6	1610	1310	192	208	103	3.4	2.1	5.4
	187	1.6	1610	1270	200	208	110	3.3	1.5	7.0
7	<u>EMI-AFB - 2; chamber volume 60 cm³; positive center electrode</u>									
	160	1.6	1750	1480	200	250	112	1.1	0.9	3.6
	161	1.6	1750	1480	200	253	108	1.1	1.5	5.6
	162	1.6	1750	1440	200	248	110	1.1	3.5	4.0
	163	1.6	1750	1440	205	253	110	1.1	2.5	5.0
	164	1.6	1750	1420	197	248	115	1.1	4.9	2.2
8	<u>EMI-AFB - 2; chamber volume 100 cm³; positive center electrode</u>									
	53	1.6	1750	1340	175	235	140	2.4	4.3	11.7
	70 ^a	1.6	1750	1400	180	235	118	2.3	4.5	7.2
	71 ^a	1.6	1750	1440	172	230	112	3.7	4.8	8.3
	74	1.6	1750	1480	185	235	114	1.8	5.2	11.7
	77	1.6	1750	1530	165	225	130	1.9	2.15	10.0
	78	1.6	1750	1440	165	227	118	2.1	0.3	12.0

a: Incomplete combustion; b: Rupture disk limits p_{max} ; c: Materials failure;
d: No ignition

Table 3. Results of test firings (continued)

Test Set	Test No.	Vent Orifice Diam. [mm]	U_L [V]	U_{max} [V]	I_{max} [A]	P_{max} [kW]	E_{max} [I]	$t_{10\%}$ [ms]	$t_{90-10\%}$ [ms]	P_{max} [MPa]
9	<u>EMI-AFB - 2; chamber volume 60 cm³; negative center electrode</u>									
	165	1.6	1580	1000	208	195	200	3.1	2.2	4.7
	166 ^a	1.6	1590	960	208	198	120	3.2	1.8	1.4
	167	1.6	1600	950	205	186	200	3.0	1.4	7.6
	168	1.6	1610	980	210	200	210	3.4	2.3	7.5
	169	1.6	1620	1000	215	207	205	3.8	1.9	6.5
	170 ^d	1.6	1650	1020	217	215	215	--	--	--
10	<u>EMI-AFB - 2; chamber volume 100 cm³; negative center electrode</u>									
	188 ^d	1.6	1610	1005	218	210	199	--	--	--
	189 ^a	1.6	1610	965	211	197	169	5.2	1.6	2.4
	190	1.6	1600	920	215	190	185	7.5	2.4	9.0
	191 ^a	1.6	1600	900	216	188	181	8.8	2.2	2.8
	192	1.6	1600	920	206	194	180	7.2	1.6	7.5
11	<u>EMI-AFB - 3; chamber volume 60 cm³; positive center electrode</u>									
	155 ^d	1.6	1780	1780	165	240	39	--	--	--
	156 ^c	1.6	1830	1820	175	260	48	1.2	3.2	15.0 ^b
	157 ^c	1.6	1830	1780	165	250	43	1.0	2.2	6.9
	158 ^a	1.6	1830	1750	160	242	51	2.9	4.0	3.0
	169 ^c	1.6	1830	1700	140	220	68	1.2	1.2	9.5
	177 ^d	1.6	1830	1840	165	252	44	--	--	--
12	<u>EMI-AFB - 3; chamber volume 100 cm³; positive center electrode</u>									
	117	1.6	1750	1750	152	225	43	3.8	1.4	11.0
	118	1.6	1750	1720	165	238	50	6.6	3.4	15.0
	120	1.6	1750	1750	155	225	45	9.0	2.5	14.8
	124	1.6	1770	1710	168	240	49	5.1	1.7	11.0
	130 ^c	1.4	1800	1770	145	320	58	1.5	2.4	11.7
	132 ^c	1.4	1800	1800	165	245	38	1.1	4.5	7.8
	137 ^c	1.4	1780	1780	168	238	28	1.2	3.1	8.0
	139 ^a	1.5	1780	1750	175	140	44	1.2	3.6	7.9

a: Incomplete combustion; b: Rupture disk limits P_{max} ; c: Materials failure;
d: No ignition

Table 3. Results of test firings (continued)

Test Set	Test No.	Vent Orifice Diam. [mm]	U_L [V]	U_{max} [V]	I_{max} [A]	P_{max} [kW]	E_{max} [I]	$t_{10\%}$ [ms]	$t_{90-10\%}$ [ms]	P_{max} [MPa]
13	<u>EMI-AFB - 3; chamber volume 100 cm³; negative center electrode</u>									
	143	1.5	1600	1490	179	210	75	1.8	6.8	5.6
	144	1.5	1620	1410	180	212	82	3.0	4.1	8.4
	145 ^c	1.5	1630	1350	190	212	102	1.8	5.6	6.0
	146 ^a	1.6	1630	1450	184	220	80	1.7	3.6	6.4
	152 ^c	1.5	1610	1410	192	215	82	2.8	2.0	10.3
	153 ^c	1.5	1610	1440	187	215	76	1.2	2.2	8.0
14	<u>EMI-AFB - 3; chamber volume 60 cm³; negative center electrode</u>									
	171	1.6	1610	1400	195	220	85	2.8	2.5	12.2
	172 ^c	1.6	1610	1300	198	217	89	3.9	3.7	8.4
	173 ^c	1.6	1610	1500	173	210	67	0.9	1.5	4.3
	174 ^a	1.6	1610	1380	185	215	96	4.0	2.7	4.6
	175 ^{ac}	1.6	1610	1310	189	212	105	3.1	2.2	6.7
15	<u>EMI-AFB - 4a; chamber volume 100 cm³; negative center electrode</u>									
	202 ^c	1.5	1550	1080	219	176	93	1.8	1.5	6.8
	203 ^c	1.5	1530	1140	209	178	94	2.4	1.4	8.4
	204 ^a	1.5	1510	970	213	165	97	2.5	6.5	0.6
	205 ^a	1.5	1520	1000	214	169	96.7	3.0	6.0	0.9
	206 ^a	1.5	1530	1000	218	169	99.4	2.7	4.8	1.01
	207 ^a	1.5	1540	980	219	173	101	6.2	3.4	16.4
16	<u>EMI-AFB - 4a; chamber volume 100 cm³; positive center electrode</u>									
	208 ^c	1.5	1700	1520	219	258	65.6	4.1	2.4	7.8
	209 ^c	1.5	1680	1540	193	250	61.3	1.7	1.0	6.3
	210 ^d	1.5	1680	1584	197	244	53.0	--	--	0.2
	211 ^d	1.5	1690	1584	210	258	65.6	--	--	0.1
	212 ^c	1.5	1690	1560	212	254	57.4	2.4	1.9	7.8
	213 ^d	1.5	1690	1584	207	254	55.2	--	--	0.2

a: Incomplete combustion; b: Rupture disk limits P_{max} ; c: Materials failure;
d: No ignition

Table 3. Results of test firings (continued)

Test Set	Test No.	Vent Orifice Diam. [mm]	U_L [V]	U_{max} [V]	I_{max} [A]	P_{max} [kW]	E_{max} [I]	$t_{10\%}$ [ms]	$t_{90-10\%}$ [ms]	P_{max} [MPa]
17	<u>EMI-AFB - 4b; chamber volume 100 cm³; positive center electrode</u>									
	214 ^d	1.6	1700	1662	171	230	41.4	--	--	0.2
	215 ^d	1.6	1720	1686	161	224.5	38.9	--	--	0.1
	216 ^c	1.6	1800	1772	163	242	39.6	1.1	1.2	7.7
	217 ^d	1.6	1800	1772	163	239	39.2	--	--	0.1
18	<u>DNAG-EMI-AFB - 5a (rough); chamber volume 100 cm³; positive center electrode</u>									
	218 ^c	1.5	1670	1440	178	210	94.1	1.6	1.9	6.2
	219 ^c	1.5	1680	1670	165	225	40	1.5	1.2	6.1
	220 ^c	1.5	1660	1450	163	215	77	1.5	0.6	6.2
	221 ^a	1.5	1650	1450	164	215	72	1.4	1.5	5.4
	222 ^c	1.5	1660	1450	165	220	69	2.6	2.7	6.1
	223 ^c	1.5	1660	1460	163	220	74	2.7	1.75	6.1
19	<u>DNAG-EMI-AFB - 5a (rough); chamber volume 100 cm³; negative center electrode</u>									
	224 ^c	1.5	1520	1000	196	193	110	3.9	1.4	7.7
	226 ^c	1.5	1520	1060	200	190	93	1.7	2.2	5.65
	227 ^d	1.5	1520	900	208	172	79	--	--	--
	228	1.5	1520	920	206	175	115	7.2	1.2	9.3
20	<u>DNAG-EMI-AFB - 5b (medium); chamber volume 100 cm³; positive center electrode</u>									
	229 ^c	1.5	1660	1430	175	225	79	1.4	1.35	5.3
	230 ^c	1.5	1640	1380	176	230	83	1.2	0.4	3.5
	231 ^c	1.5	1620	1500	145	192	69	1.5	2.4	6.6
	232 ^a	1.5	1620	1480	160	207	72	1.6	3.4	4.2
	233 ^d	1.5	1620	940	320	156	37	--	--	--
	234 ^a	1.5	1620	1420	178	220	79	1.95	1.55	2.1
21	<u>DNAG-EMI-AFB - 5b (medium); chamber volume 100 cm³; negative center electrode</u>									
	235	1.5	1540	1020	200	195	88	4.25	2.25	9.3
	236 ^c	1.5	1500	950	200	167	104	1.95	1.55	2.1
	237 ^b	1.5	1500	700	235	144	84	--	--	--
	238	1.5	1500	900	195	165	114	7.5	2.0	4.0

a: Incomplete combustion; b: Rupture disk limits P_{max} ; c: Materials failure;
d: No ignition

Table 3. Results of test firings (continued)

Test Set	Test No.	Vent Orifice Diam. [mm]	U_L [V]	U_{max} [V]	I_{max} [A]	P_{max} [kW]	E_{max} [I]	$t_{10\%}$ [ms]	$t_{90-10\%}$ [ms]	P_{max} [MPa]
22	<u>DNAG-EMI-AFB - 5c (fine); chamber volume 100 cm³, positive center electrode</u>									
	239 ^c	1.5	1620	1400	181	226	83	1.59	1.83	6.8
	240 ^d	1.5	1640	1505	204	238	57	--	--	--
	241 ^d	1.5	1600	1450	198	220	53.5	--	--	--
	242	1.5	1630	1500	230	232	56.5	2.8	1.5	11.1
	243 ^c	1.5	1630	1550	178	220	48.1	3.2	1.9	9.1
	244 ^c	1.5	1630	1530	208	234	51.8	1.6	1.9	6.4
	245 ^c	1.5	1630	1580	178	220	42	1.78	1.67	7.0
	246 ^c	1.5	1630	1560	165	214	49.3	1.4	1.28	6.5
23	<u>DNAG-EMI-AFB - 5c (fine); chamber volume 100 cm³; negative center electrode</u>									
	247 ^c	1.5	1520	950	215	165	104	4.1	1.33	8.0
	248 ^c	1.5	1520	1100	212	187	90	2.35	1.25	6.1
	249 ^a	1.5	1520	1020	218	175	95	1.9	7.1	0.7
	250 ^c	1.5	1520	930	218	163	103	4.1	3.1	6.3
24	<u>EMI-AFB - 3 SG; chamber volume 100 cm³; positive center electrode</u>									
	252 ^d	1.5	1780	1710	127	197	34	--	--	--
	253 ^a	1.5	1650	1580	122	178	34	3.8	5.4	1.4
	254 ^d	1.5	1600	1140	78	87	5.5	--	--	--
	255 ^c	1.5	1650	1580	92	135	53	4.4	2.6	7.9
	256 ^d	1.5	1650	1360	92	126	12.5	--	--	--
	257 ^d	1.5	1650	1605	72	110	22	--	--	--

a: Incomplete combustion; b: Rupture disk limits P_{max} ; c: Materials failure;
d: No ignition

3.1.1 Electrical Characteristics

Plots of current and voltage versus time were recorded for each test, as stated. Also, in many cases plots of current versus voltage were generated from the primary $I(t)$ and $U(t)$ data. Figures 25a to 25c and 26a to 26c show typical examples of such plots for the igniter configurations BRL(m/s) and EMI-AFB-3, respectively.

While the voltage rises quickly to its maximum within 0.8 ms and remains almost constant afterwards, the current is interrupted roughly at the same time that U_{\max} is reached. The earlier explanation that the interruption of the current is due to vapor sheath formation on the electrode surface, which acts as an insulator [10], is one interpretation. An alternative is that the igniter is simply charged to full capacity in analogy to an electrolytic capacitor. This, however, would imply an exponential current decay which is not observed. A more likely interpretation is a saturation of the electrode surfaces (polarization).

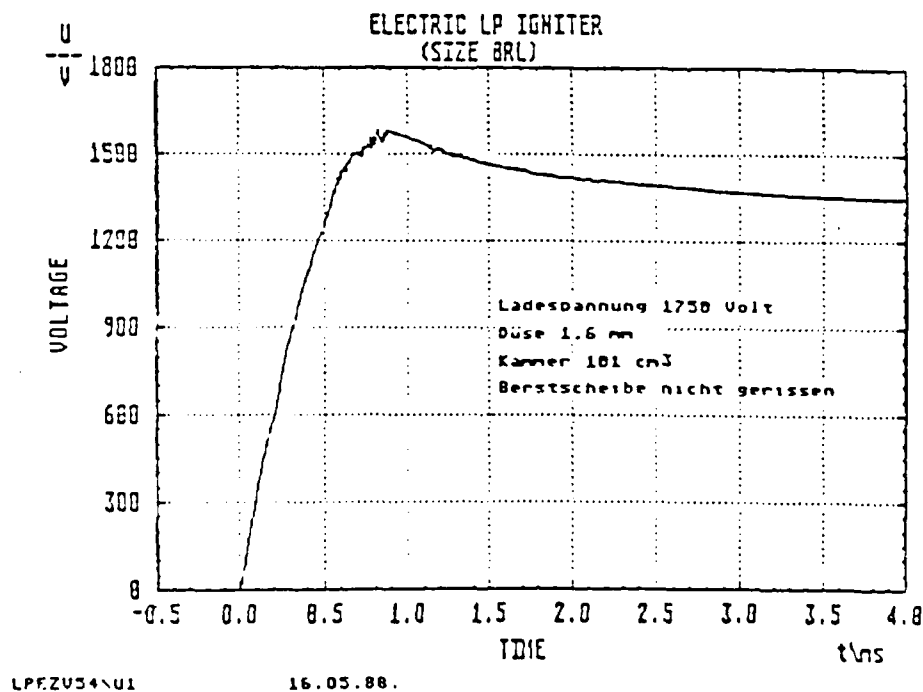


Fig. 25a. Electrical characteristics of igniter BRL(m/s); chamber volume 100 cm³; center electrode polarity (+); voltage versus time.

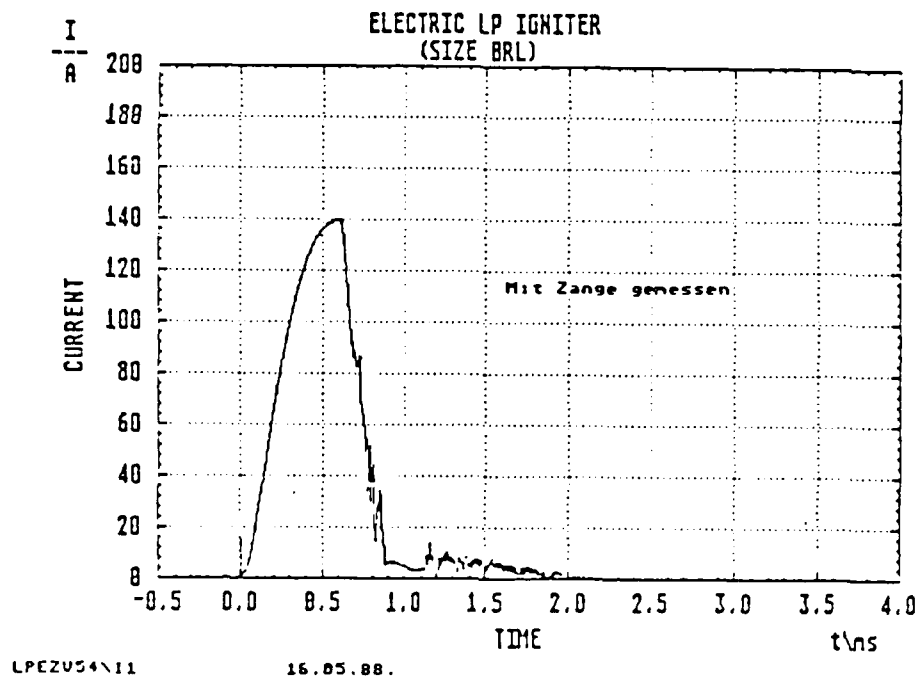


Fig. 25b. Electrical characteristics of igniter BRL(m/s); chamber volume 100 cm³; center electrode polarity (+); current versus time.

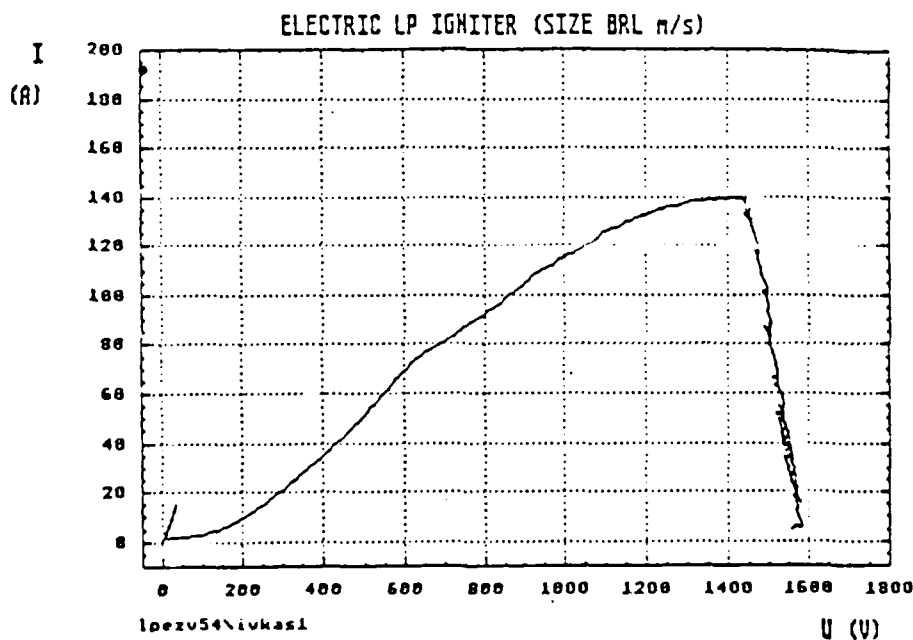


Fig. 25c. Electrical characteristics of igniter BRL(m/s); chamber volume 100 cm³; center electrode polarity (+); current versus voltage.

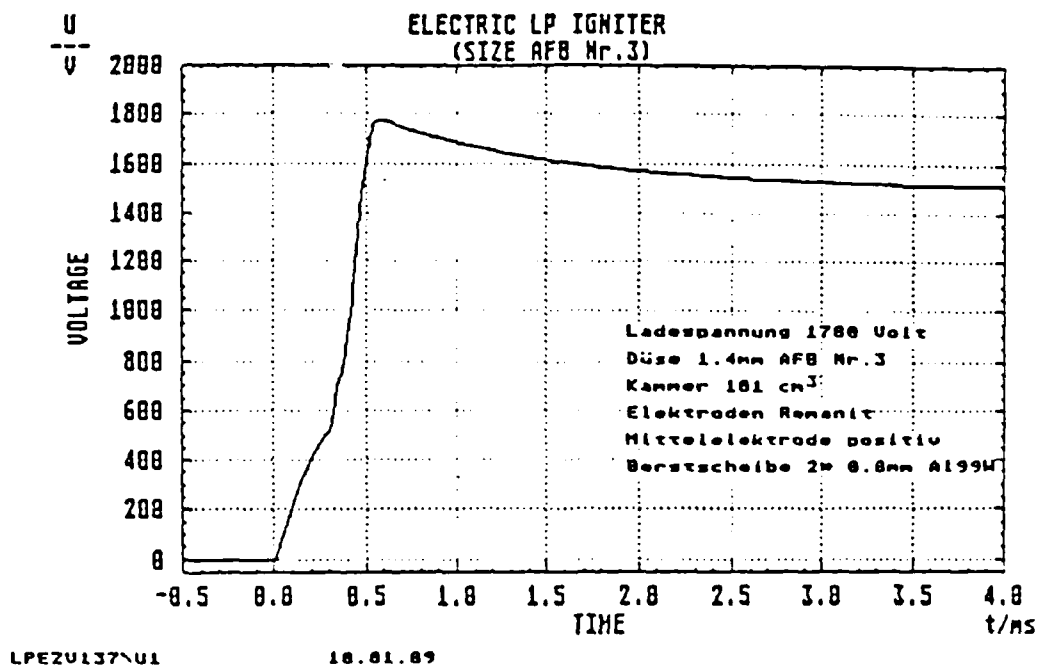


Fig. 26a. Electrical characteristics of igniter EMI-AFB-3; chamber volume 100 cm³; center electrode polarity (+); voltage versus time.

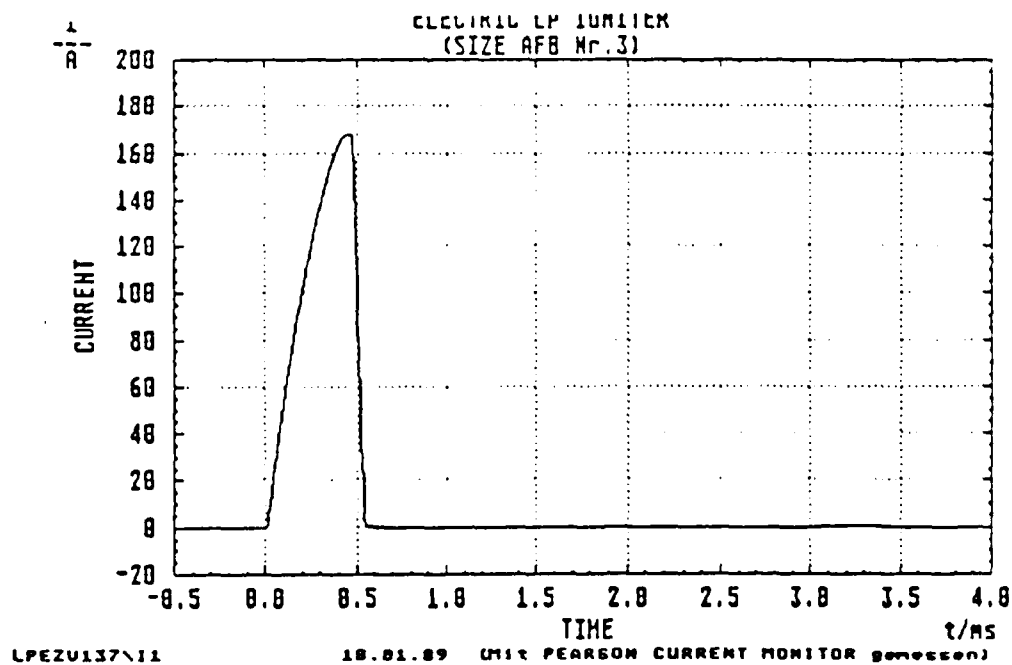


Fig. 26b. Electrical characteristics of igniter EMI-AFB-3; chamber volume 100 cm³; center electrode polarity (+); current versus time.

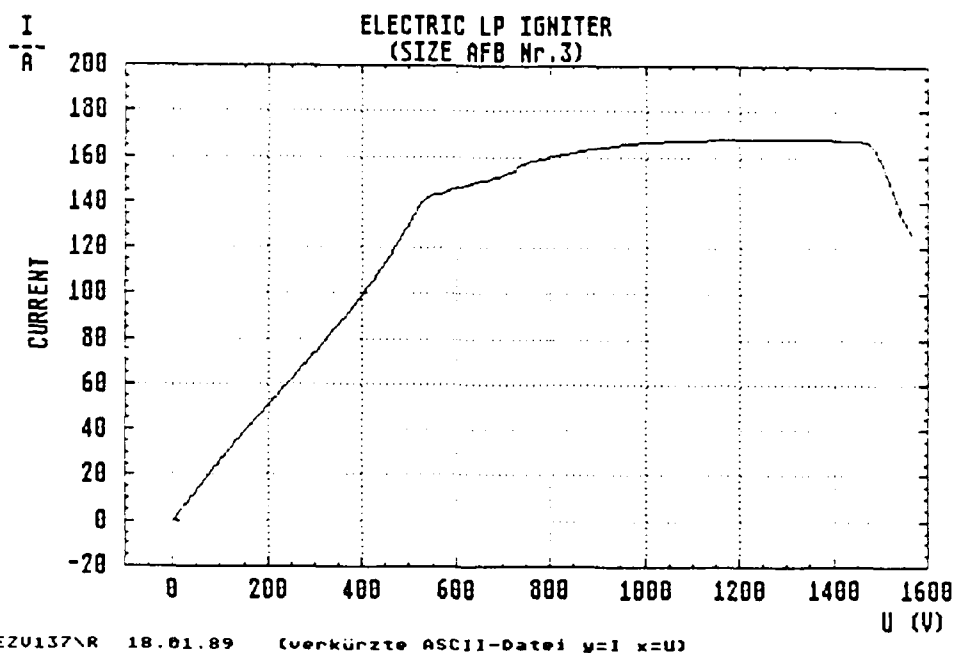


Fig. 26c. Electrical characteristics of igniter EMI-AFB-3; chamber volume 100 cm³; center electrode polarity (+); current versus voltage.

In addition, it is seen that initially there is a nearly linear relationship between I and U ; the slope is, of course, $1/R$. The absolute value of the initial ohmic resistance is characteristic for each igniter; the BRL type igniter, for example, has a resistance of about 10 Ω compared to the 3.6 to 4.0 Ω of EMI-AFB-3. Typical current versus voltage plots for other igniters are displayed in Figure 27.

The $I(U)$ plots, although characteristic for the igniter configuration used, have some features in common. At first, the initial portion of the curves is linear as in an ohmic circuit where no additional electrochemical conversions or charge transfers are taking place on the electrodes. Secondly, the curves flatten out shortly before the conductivity breaks down. As yet, it is not clear whether or not this "saturation" should result from some undisclosed electrode polarization effects. On the other hand, given the voltage gradients achieved with the existing test setup, vapor sheath formation should induce arc ignition, which generally did not occur in our tests.

For reference purposes, a series of ignition tests were carried out with an inert 0.73 M KCl solution placed inside the cavity instead of liquid propellant. The igniter was EMI-AFB-3. At room temperature the specific conductance of 0.73 molar (M) KCl ($\kappa = 0.08 \Omega^{-1}\text{cm}^{-1}$) matches that of LGP 1846.

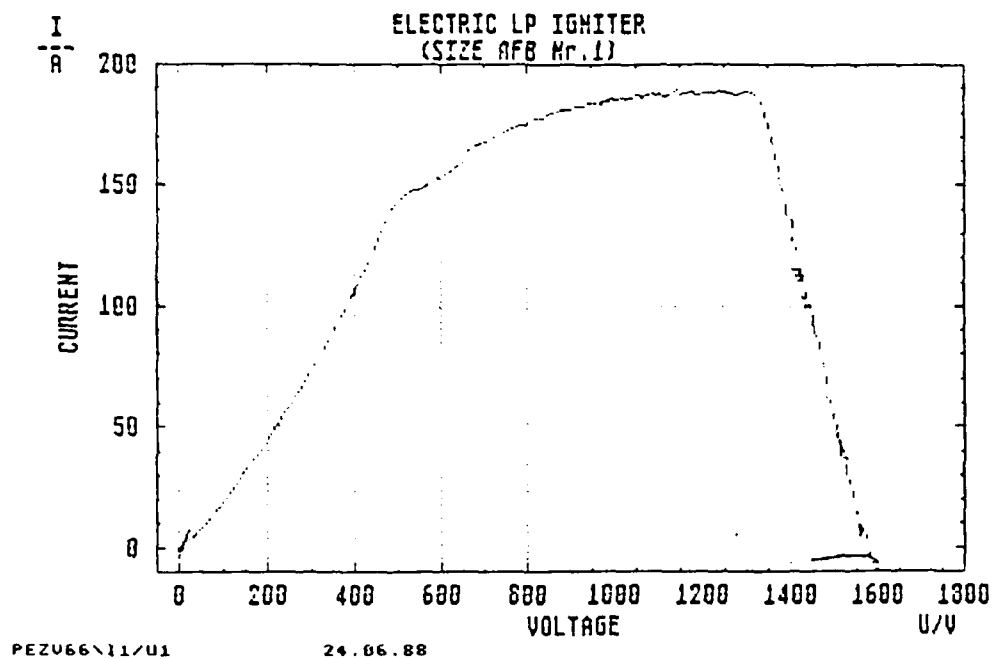


Fig. 27a. Plot of current versus voltage of igniter EMI-AFB-1; chamber volume 100 cm³; center electrode polarity (+).

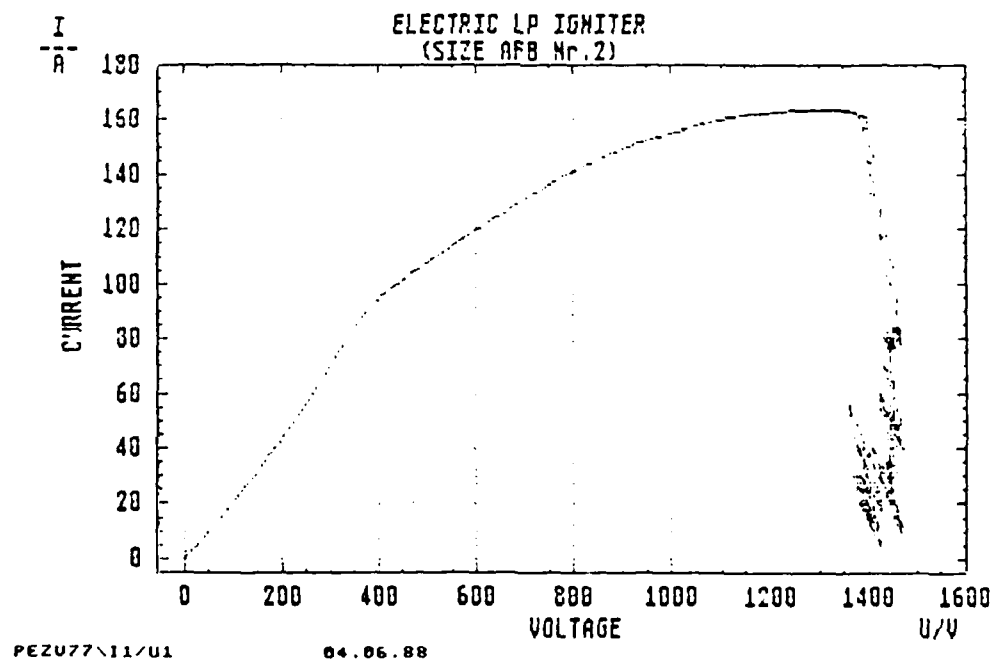


Fig. 27b. Plot of current versus voltage of igniter EMI-AFB-2; chamber volume 100 cm³; center electrode polarity (+).

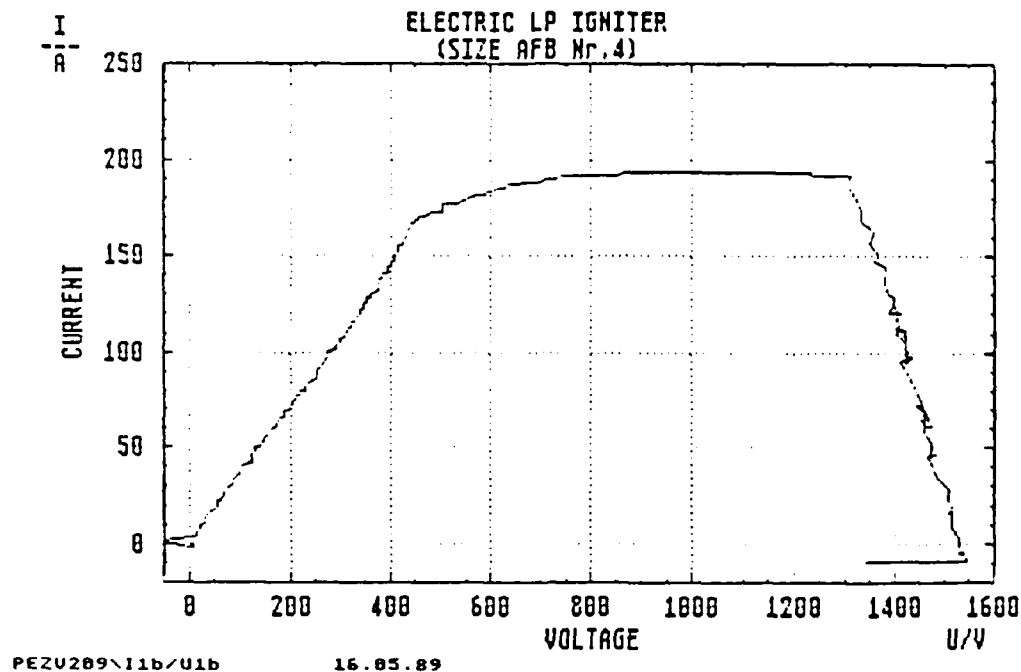


Fig. 27c. Plot of current versus voltage of igniter EMI-AFB-4; chamber volume 100 cm³; center electrode polarity (+).

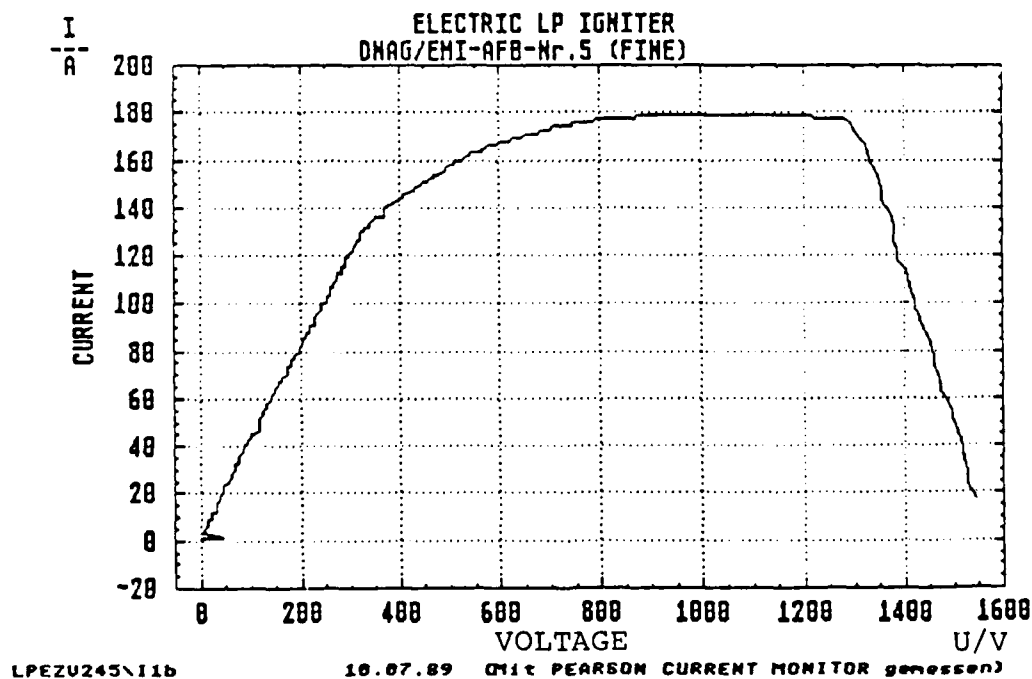
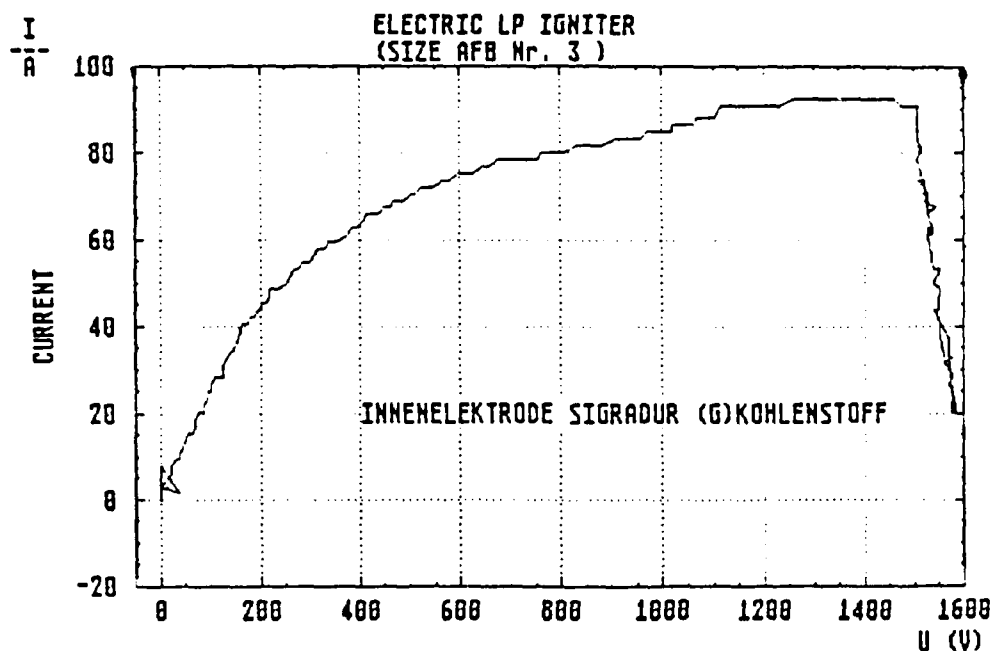


Fig. 27d. Plot of current versus voltage of igniter DNAG-EMI-AFB-5c; chamber volume 100 cm³; center electrode polarity (+).



LPE2U255\R 29.08.89

Fig. 27e. Plot of current versus voltage of igniter EMI-AFB-3 SG; chamber volume 100 cm³; center electrode polarity (+).

The initial ohmic resistance taken from Figure 28c is 3.6 Ω , which is identical to the value observed for the liquid propellant charge. Despite a significantly lower charge voltage, 1200 V for KCl versus 1600+ V for LGP 1846, electric arc formation between the electrodes occurred at $U_{\max} = 1000$ V as seen in Figures 28a and 28b. The voltage drops at $t \approx 1.0$ ms whereas the current surges.

On reversal of the electrode polarity somewhat different electrical behavior is observed, as seen from the comparison of Figures 26 and 29. The I versus U plot in Figure 29c actually shows a current "step" following the initial ohmic portion of the curve. Moreover, as will be demonstrated below, the charge voltage needed for ignition is lower while the energy consumed is raised when switching from positive to negative center electrode polarity. A simple RLC circuit should not show any polarity effect.

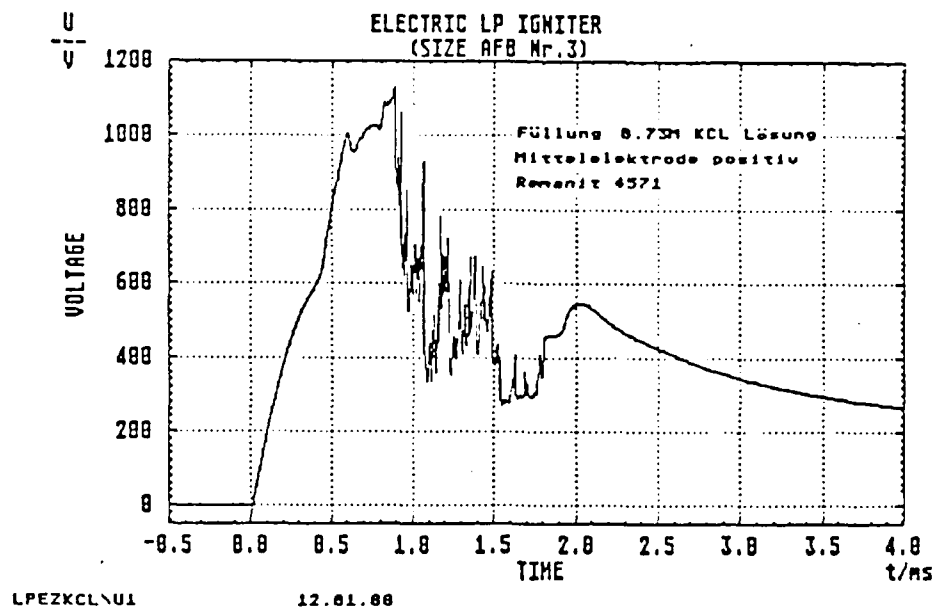


Fig. 28a. Electrical characteristics of igniter EMI-AFB-3 with electrolyte 0.73 M KCl; chamber volume 100 cm³; center electrode polarity (+); voltage versus time. Here arc discharge occurs at about $t = 0.9$ ms.

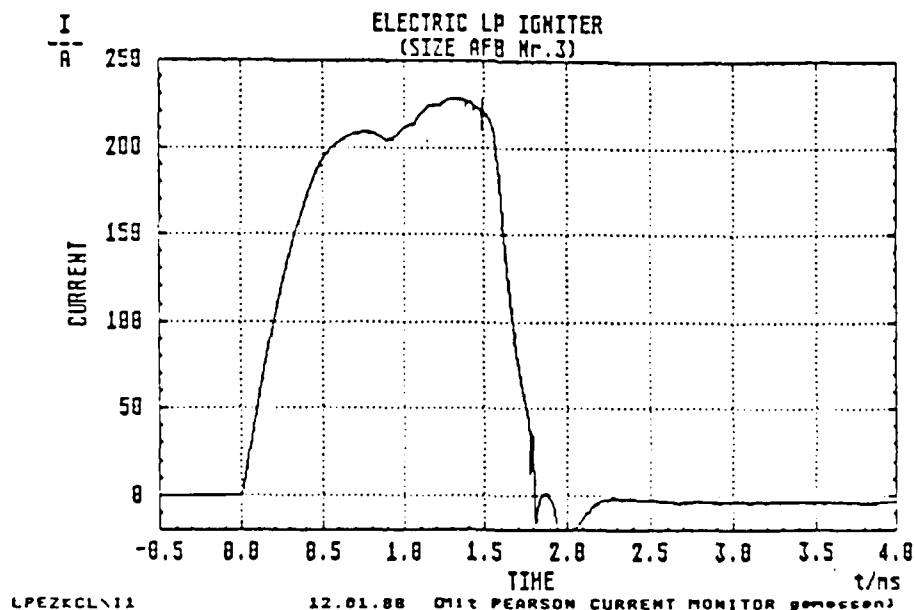


Fig. 28b. Electrical characteristics of igniter EMI-AFB-3 with electrolyte 0.73 M KCl; chamber volume 100 cm³; center electrode polarity (+); current versus time. Here arc discharge occurs at about $t = 0.9$ ms.

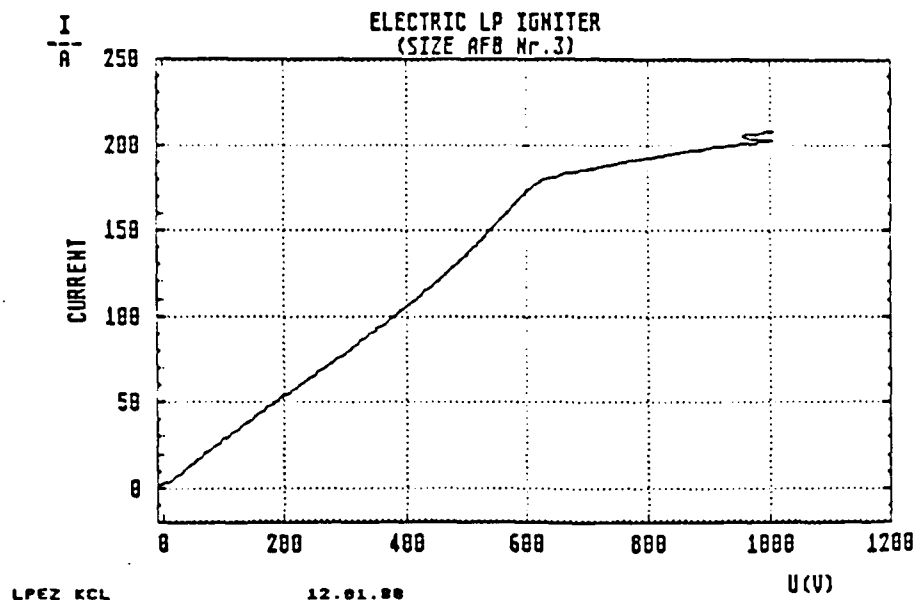


Fig. 28c. Electrical characteristics of igniter EMI-AFB-3 with electrolyte 0.73 M KCl; chamber volume 100 cm³; current versus voltage.

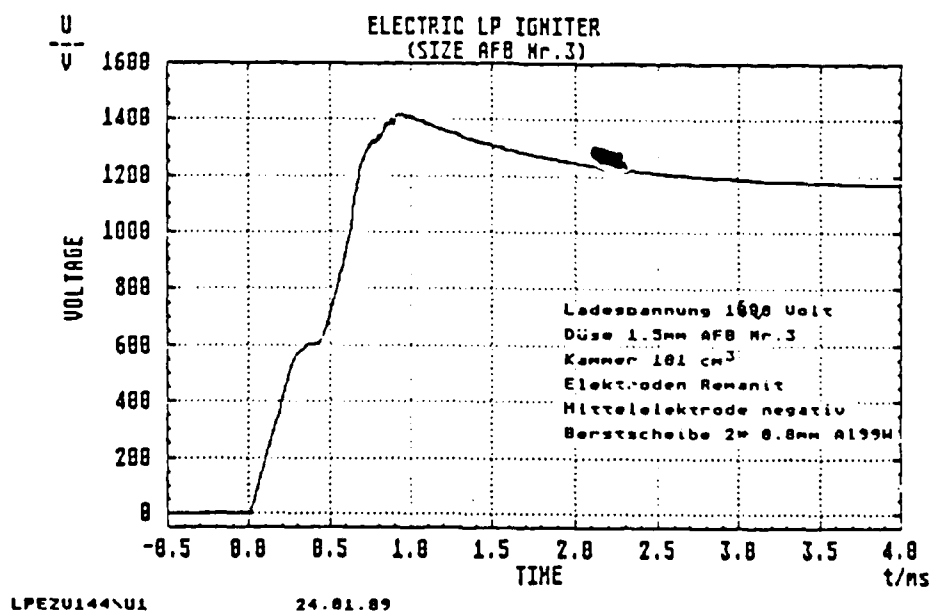


Fig. 29a. Electrical characteristics of igniter EMI-AFB-3; chamber volume 100 cm³; center electrode polarity (-); voltage versus time.

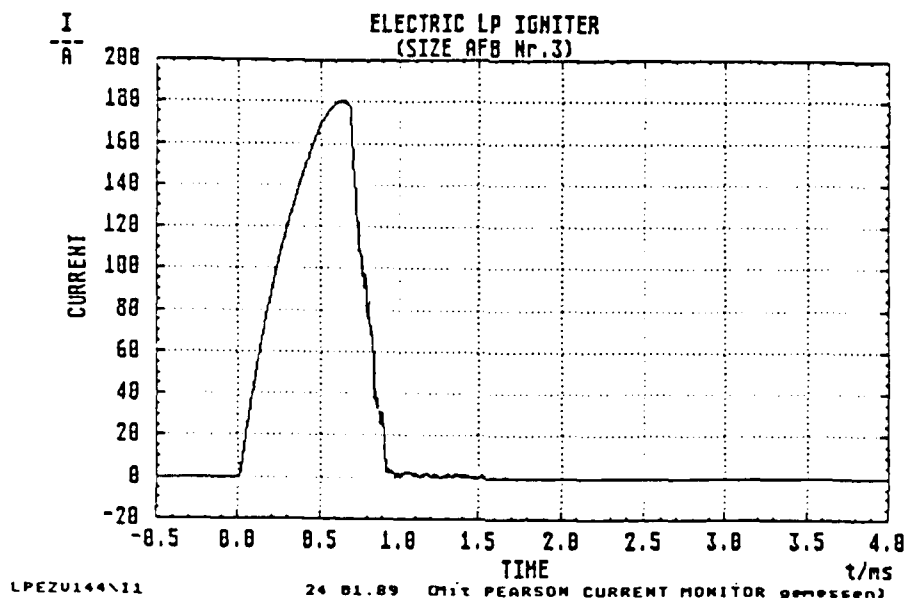


Fig. 29b. Electrical characteristics of igniter EMI-AFB-3; chamber volume 100 cm^3 ; center electrode polarity (-); current versus time.

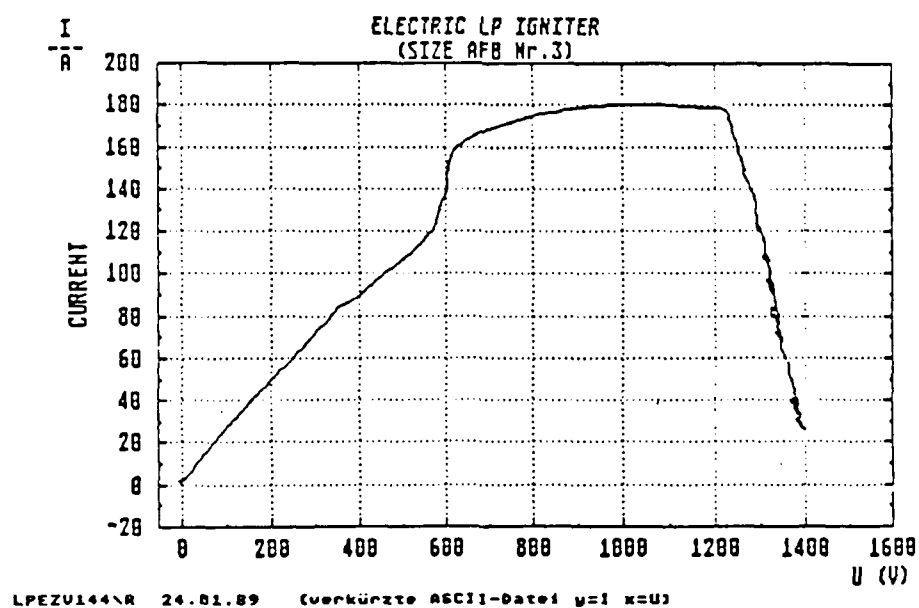


Fig. 29c. Electrical characteristics of igniter EMI-AFB-3; chamber volume 100 cm^3 ; center electrode polarity (-); current versus voltage.

3.1.2 Effect of Chamber Volume

A definite correlation exists between the test chamber volume, i.e., the gas expansion volume, and the ignition delay time, $t_{10\%}$. Other parameters remaining constant, the longer $t_{10\%}$ is observed for the larger chamber volume, 100 cm³, as compared to 60 cm³. This is seen most clearly by comparing the average $t_{10\%}$ value from sets 7 to 12 of Table 3. The averages are tabulated in Table 4. The averaged maximum voltages in Table 4 differ by not more than 50 V. The vent diameter was 1.6 mm throughout.

Table 4. Effect of chamber volume on average ignition delay, $\bar{t}_{10\%}$

Electrode Configuration	Test Set (Tables)	Chamber Volume [cm ³]	Polarity Center Electrode	\bar{U}_{\max} [V]	$\bar{t}_{10\%}$ [ms]
EMI-AFB - 2	7	60	+	1452	1.1
	8	100	+	1438	2.4
EMI-AFB - 2	9	60	-	978	3.4
	10	100	-	926	7.2
EMI-AFB - 3	11	60	+	1762	1.1
	12	100	+	1740	6.1

It should be noted, however, that there was considerable scatter in the $t_{10\%}$ values as seen in the plots of $t_{10\%}$ versus U_{\max} in Figures 30a and 30b. In part this is caused by the superposition of changes in other parameters (see below). Nevertheless, the results from Table 4 are supported by these two plots, in that the $t_{10\%}$ values are larger for the 100 cm³ chamber than for the 60 cm³ chamber. The scattering is more pronounced in the values from the larger volume. The same overall behavior was also found for the EMI-AFB-1 geometry. For BRL(m/s) there are not enough values taken with the same vent diameter to permit a comparison.

It is known from tests with incomplete combustion that a certain amount of liquid propellant is first blown out of the igniter before burning has taken place. Thus, given that the liquid propellant is not totally combusted at the time it exits from the igniter into the expansion volume, it seems plausible that combustion would be retarded in the larger volume. The chamber volume apparently plays a part in the confinement of the liquid propellant.

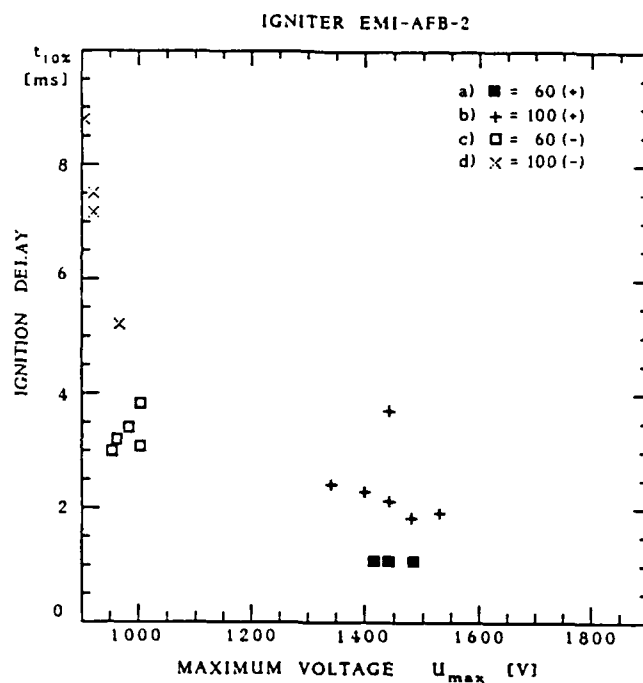


Fig. 30a. Ignition delay, $t_{10\%}$, versus maximum voltage, U_{\max} [V] of igniter EMI-AFB-2; chamber volumes 60 and 100 cm^3 ; center electrode polarities (+) and (-).

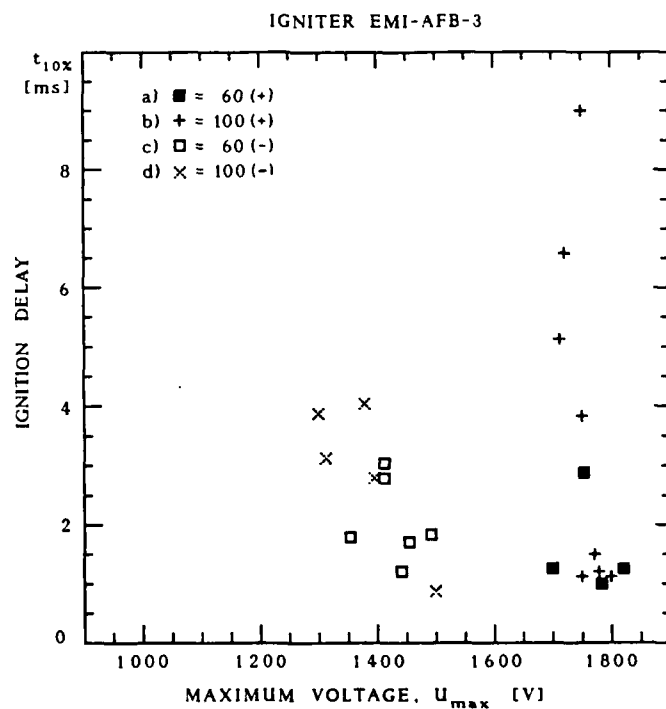


Fig. 30b. Ignition delay, $t_{10\%}$, versus maximum voltage, U_{\max} [V] of igniter EMI-AFB-3; chamber volumes 60 and 100 cm^3 ; center electrode polarities (+) and (-).

The best igniter performance achieved a pressure of about 15 MPa in the 100 cm³ chamber. This is only 60% of the expected value of 25 MPa calculated for an adiabatic flame under adiabatic system conditions. The heat loss of the system was not determined. The pressure buildup should be sufficiently high, however, to start the regenerative injection process in a 30-mm RLPG with an initial combustion chamber volume of 20 cm³ and a total volume of about 60 to 70 cm³.

3.1.3 Effect of Vent Diameter

As mentioned in the last section, Figures 30a and 30b show scattering of the ignition delay versus the chamber volume size. In the case of the EMI-AFB-3 igniter results shown in Figure 30b, this is most prominent for the 100 cm³ chamber volume and a positive center electrode. A look at test set 12 of Table 3 and the plot of $t_{10\%}$ against vent diameter in Figure 31 reveals that the vent diameter of the outer electrode plays an important part in the control of the ignition process. Generally, there is an increase of $t_{10\%}$ with the vent diameter. In other words, the confinement is determined to a great extent by the vent diameter, as expected.

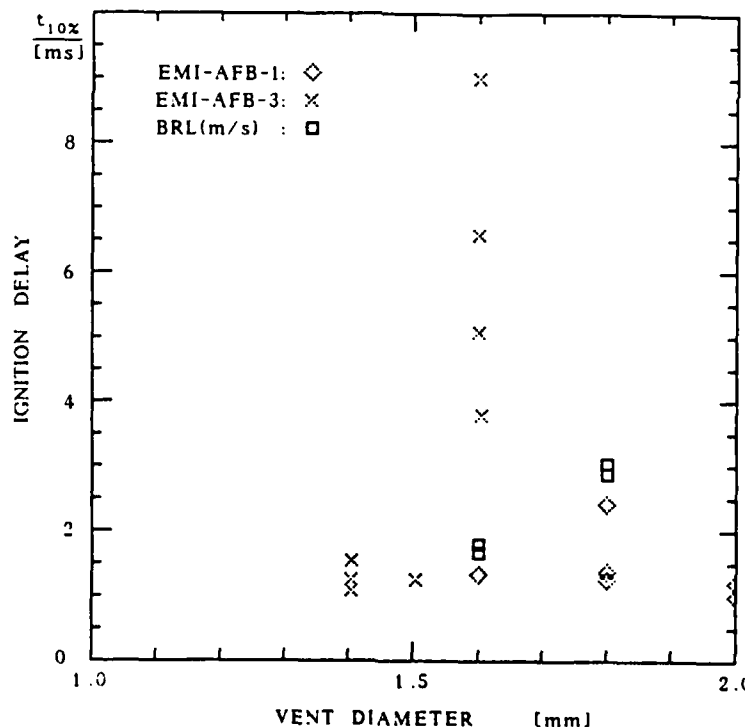


Fig. 31. Ignition delay, $t_{10\%}$, versus vent diameter.

The EMI-AFB-1 igniter (Test set 4, Table 3) seems to be an exception. It is possible that different igniter geometries exhibit different sensitivities towards the vent diameter. However, it should be recalled that the vent diameter is less important a factor for the smaller 60 cm³ chamber as was the case for the tests in question. Even so the ignition delay times seem rather erratic; on the other hand, the vent diameters of 1.8 and 2 mm used in these tests are at the upper limit for successful ignition, since larger vent sizes result in unsuccessful ignition. The ignition delay times are expected to become less controllable when the vent diameter is increased to its maximum value.

3.1.4 Effect of Polarity/Voltage

A switch in polarity of the center electrode from positive to negative results in a considerable increase of the energy consumed during the discharge by a factor of about 1.8. What is more, the ignition delay time, $t_{10\%}$, is substantially increased as is clearly visible from Figures 30a and 30b while the charge voltage necessary for ignition was decreased. This effect is more pronounced for the large 100 cm³ volume than the 60 cm³ volume.

The plots of energy consumption versus maximum voltage in Figures 32 and 33 show linear correlation between the two variables. Surprisingly, energy consumption diminishes with increased maximum voltage. Further, different geometries are located along a single line. Performing least squares analysis of the data in Figure 33, for example, gives the following results:

Table 5. Regression analysis $E(U_{\max})$; chamber volume 100 cm³; center electrode polarity (-); data from Figures 32 and 33.

	F i g u r e s			
	32 (a)	32 (b)	33 (a)	33 (b)
A_0 [J]	447.0	309.2	362.3	192.6
A_1 [J·V ⁻¹]	-0.23	-0.16	-0.197	-0.093
r	-0.99	-0.94	-0.99	-0.77
SEE [J]	±4.8	±5.1	±5.4	±5.0
n	23	21	17	16

n: number of points

SEE: Standard Error of Estimate: $s_{y,x} = \sqrt{\frac{\sum (Y - \hat{Y})^2}{n-2}}$
 $\hat{Y} = A_0 + A_1 X$

r: correlation coefficient

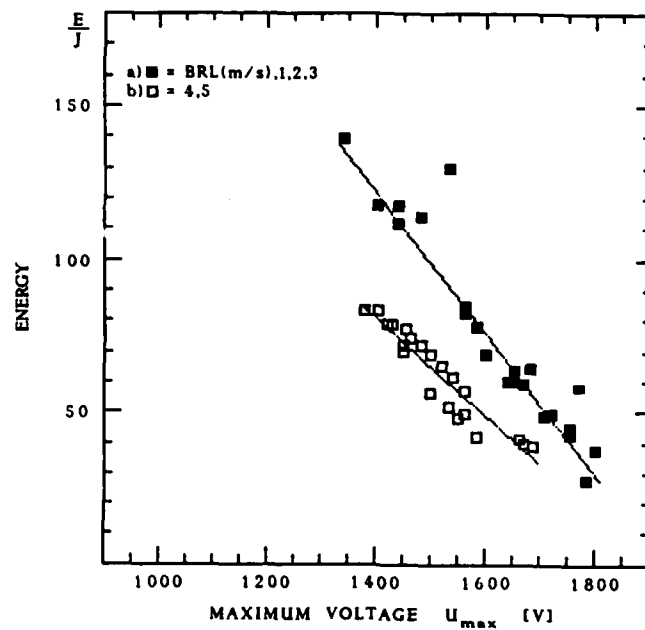


Fig. 32. Energy versus maximum voltage; chamber volume 100 cm^3 ; center electrode polarity (+); igniter configurations: (a) BRL(m/s), EMI-AFB-1,2,3; (b) EMI-AFB-4, DNAG-EMI-AFB-5

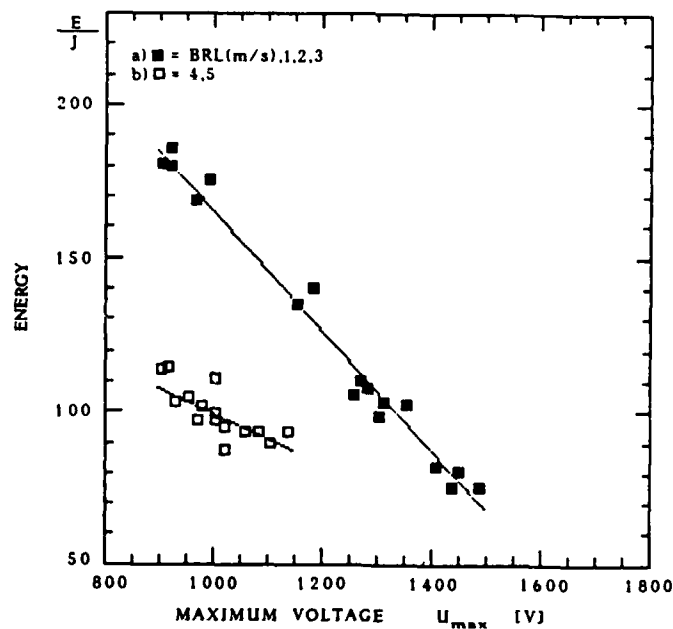


Fig. 33. Energy versus maximum voltage; chamber volume 100 cm^3 ; center electrode polarity (-); igniter configurations: (a) BRL(m/s), EMI-AFB-1,2,3; (b) EMI-AFB-4, DNAG-EMI-AFB-5

Thus, the SEE are on the order of only 5 J in both figures. This is a considerable improvement over the scatter of ± 20 J obtained previously [6,20] when only average energies were considered (see Table 6 for average energies).

Note, that in the majority of cases the charge voltage, U_L , and U_{max} values for a given igniter type varied only over a restricted range. The reason for this is that there exist both a lower and an upper "cutoff" voltage, which are specific for a given igniter geometry. Arcless ignition is successful only within these bounds. For example, consider the EMI-AFB-4a and 4b geometries. These are the same save for the parameter l_I , which is 8.2 mm and 5.2 mm, respectively. Accordingly, at a given voltage the field strength should be greater for igniter EMI-AFB-4a than 4b and so ignition should be easier in the former case. Indeed, configuration 4a requires less voltage for ignition, but - contrary to the above argument - consumes more energy. On the other hand, a correlation between energy and electrode surface area is described in Section 3.1.5.2, see Figures 36 to 38. An attempt to increase the charge voltage for the EMI-AFB-4a igniter so as to obtain the same U_{max} as for EMI-AFB-4b and thereby lower the energy consumption will instead result in unwanted arcing between the electrodes.

It is seen that at the same U_{max} the energies of the points (a) are considerably higher than the energies of the points (b) in Figures 32 and 33. This indicates that the electrode configuration DNAG-EMI-AFB-5 and its closest approximation, EMI-AFB-4, do indeed represent an optimization for energy efficient ignition.

In the light of these results it should be noted that a comparison of igniters with respect to their average energy consumption, as will be presented below, must take into account the dependence of E on U_{max} . Strictly speaking, only energies obtained with the same U_{max} should be averaged; although this was not possible within the scope of the work. Fortunately, for any given igniter configuration the measured U_{max} were usually spaced over a relatively small interval.

3.1.5 Effect of Igniter Geometry

3.1.5.1 Theoretical

As mentioned previously (see Chapter 1.4), it was expected that the field line distribution in the igniter cavity would impinge not only on the kinetics of the ignition process but also on the reproducibility of ignition as a whole.

Before proceeding with the calculation, the desired number of field lines to be displayed was set to a fixed value of 10. After completion of the calculation procedure the field lines were then spread out over the two-dimensional cross section of the igniter. Results of such calculations are shown in Figure 34a for the BRL type igniter and in Figure 34b for the EMI-AFB-1 configuration.

The figures show how the increase of the size of the outer, vented electrode affects the field line density. The distance between two field lines is indicative of the relative field strength in this segment; i.e., large distances corresponding to small field strength. As mentioned before, ignition should preferably occur in places of high field line density. Further, it is reasonable to expect that reproducibility of ignition should be improved if the ignition occurs at one site only. Figures 34a and 34b show that while both igniter types have unique and pronounced density maxima on each center electrode, there are two density maxima on each outer electrode. This is further illustrated by plotting the segment surface area versus the segment number as shown in Figure 35a.

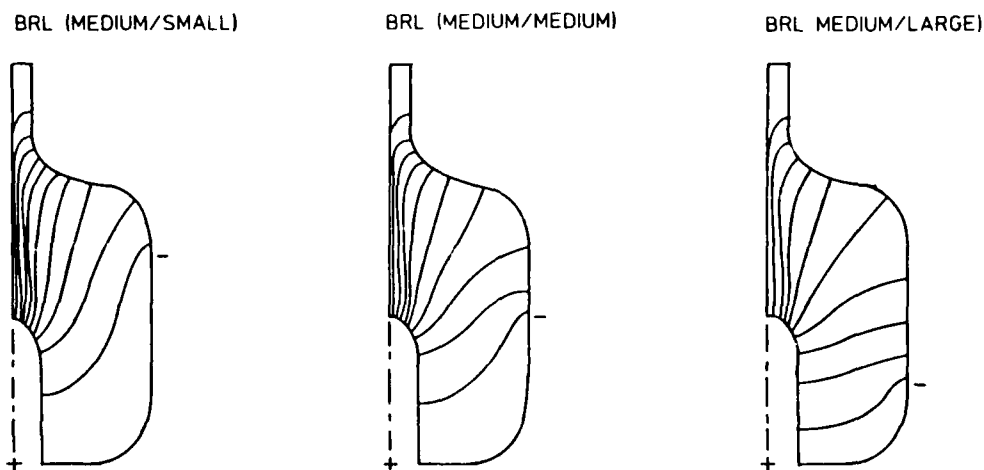


Fig. 34a. Schematic presentation of field line density for (m/s), (m/m) and (m/l) configurations; type BRL.

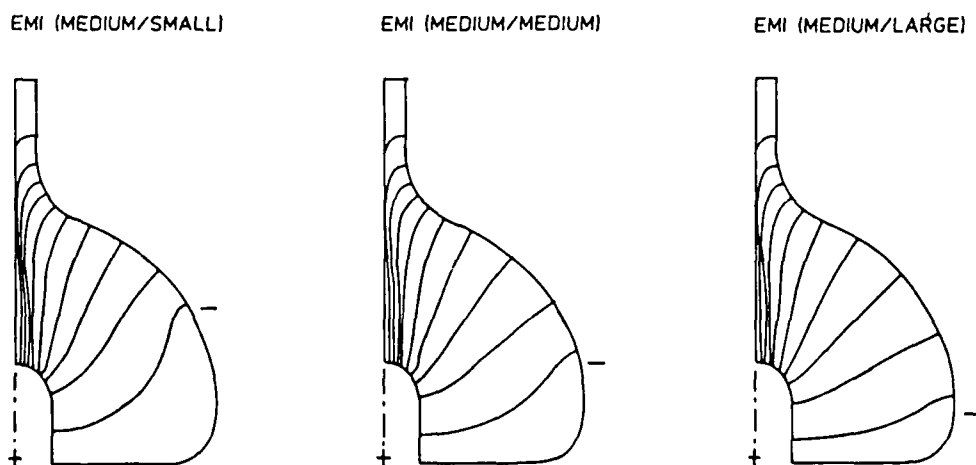


Fig. 34b. Schematic presentation of field line density for (m/s), (m/s) and (m/l) configurations; type EMI-AFB-1.

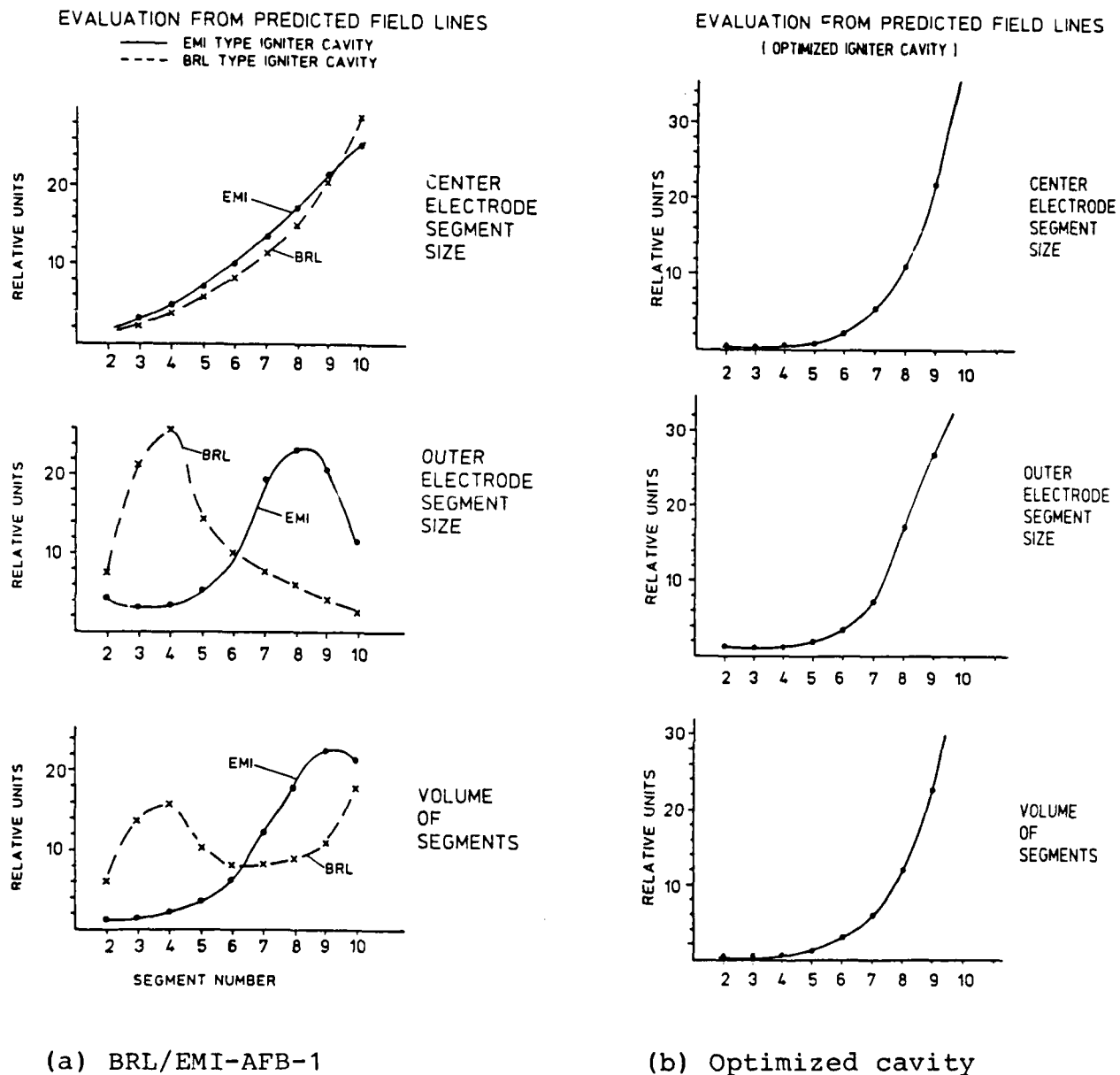


Fig. 35. Relative surface area of segments versus segment number.

An estimate of the divergence of the electric field lines at the center electrode, and hence the field line density, is also given by the ratio, Q , of the center electrode surface area divided by the outer electrode surface area. Such a correlation is presented in Section 3.1.5.2. The approximation of the electric field distribution by surface area ratio, Q , is, of course, restricted to cavity designs showing overall similarity, as is the case for the geometries studied here.

Figure 35 shows clearly that the outer electrode of the 'narrow' BRL configurations has a high field line density at low segment numbers, near the vent, and again at high segment numbers, near the outer rim. The somewhat broader EMI-AFB-3 type geometry has a less pronounced field line density maximum at the outer rim. Note that Figures 34a and 34b indicate that variations in the inner and outer electrode lengths also affect the field line density distributions. These dependencies can also be utilized for igniter optimization.

3.1.5.2 Empirical

The following presents a survey of empirical performance data; particularly, the energy absorbed and the ignition delay time with respect to geometrical parameters. One geometric quantity which initially showed some promise was the length to diameter ratio (L/D) [6,20]; the cavity length was denoted by "L" and the cavity width at the center electrode tip by "D". This was deemed to give some indication of the distribution of liquid propellant in the cavity.

It has since been demonstrated that this relationship to igniter performance had been entirely fortuitous. Indeed, igniters 4a and 4b have the same L/D ratio but, for example, distinctly different energy consumptions. Attempts at correlating the average energy consumption, E , and the ignition delay, $t_{10\%}$, to the electrode surface areas, A_{si} , A_{so} , as well as the area ratio, Q , have been more successful. These data are summarized in Table 6. There was no discernible effect of the chamber volume on energy consumption [20]; for this reason, the plots shown below do not include the values for the 60 cm³ chamber.

The finding presented in Section 3.1.4, namely that E correlates inversely with U_{max} , seems to indicate that the electrode/cavity geometry or the field line distribution is not so important as far as the energy consumption is concerned, at least when comparing configurations situated on the same regression line (Figures 32 and 33) of E versus U_{max} . On the other hand, the configurations EMI-AFB-4 and DNAG-EMI-AFB-5 absorb substantially less energy than the others. Also, the igniter shape determines the location of the interval of permitted U_{max} values in which arcless ignition occurs.

Generally, E is seen to rise proportionally with center electrode surface area and inversely with outer electrode surface area. A better correlation is observed between E and the surface ratio, Q , as shown in Figures 36 to 38. The regression coefficients of $E(Q)$ are given in Table 7. A small value of Q reflects a strongly divergent electrical field, i.e., high field line density at the center electrode tip.

Again, energy consumption is higher for a negative center electrode; the same holds true for the slope of E versus Q (Table 7). These findings, as expected, contradict the prediction of Irish's model [10] which is independent of electrode polarity. It is recalled that Carleton et al. favored the anode as initiation site for the

Table 6. Comparison of average energy consumption and ignition delay

Electrode Type	Inner Outer Electrode A _{Si} A _{So} [mm ²]		Ratio Q A _{Si} /A _{So}	Ignition Delay t _{10%} ⁺ t _{10%} ⁻ [ms]		Average Energy E ₁₀₀ ⁺ E ₁₀₀ ⁻ E ₆₀ ⁺ E ₆₀ ⁻ [J]			
BRL(m/s)	81.4	198.3	.41	2.37	3.85	76	161	90.6	--
EMI-AFB-1	56.3	400.0	.141	3.08 ¹	3.41	63	103	59.6	--
EMI-AFB-2	126.7	263.5	.481	2.37	7.2	122	187	111	203.8 ²
EMI-AFB-3	46.3	442.5	.105	6.1	2.05	44.4	79 ³	48.8	88.4
EMI-AFB-3-SG	46.3	442.5	.105	4.1 ⁴	--	33.4 ⁴	--	--	--
EMI-AFB-4a	82.4	602.0	.137	2.73	2.48 ⁵	59.7	96.9	--	--
EMI-AFB-4b	52.3	602.0	.087	1.1	--	39.9	--	--	--
DNAG-EMI-AFB-5a	82.7	506.8	.163	1.88	4.3	71 ⁶	106 ⁷	--	--
DNAG-EMI-AFB-5b	82.7	506.8	.163	1.53	4.57	76.4 ⁸	97.5 ⁹	--	--
DNAG-EMI-AFB-5c	82.7	506.8	.163	1.59 ¹⁰	3.11	49.54 ¹¹	98	--	--

Symbols:

A_{Si}/A_{So} : Surface area of inner/outer electrode

Q : Ratio A_{Si}/A_{So}

$t_{10\%}^+$: Time elapsed for 10% of maximum pressure (ignition delay), chamber volume 100 cm³; positive center electrode

$t_{10\%}^-$: Time elapsed for 10% of maximum pressure (ignition delay), chamber volume 100 cm³; negative center electrode

E_{100}^+ : Energy consumption, chamber volume 100 cm³; positive center electrode

E_{100}^- : Energy consumption, chamber volume 100 cm³; negative center electrode

E_{60}^+ : Energy consumption, chamber volume 60 cm³; positive center electrode

E_{60}^- : Energy consumption, chamber volume 60 cm³; negative center electrode

Mean values are based on results summarized in Table 3. Except where indicated, averages were taken over all test results of corresponding test sets in Table 3.

1) Tests (52, 63, 65, 67)

2) Tests (165, 167-169)

3) Tests (143, 144, 146, 152, 153)

4) Tests (253, 255-257)

5) Tests (202-206)

6) Tests (220-223)

7) Tests (224, 226, 228)

8) Tests (229-232, 234)

9) Tests (235, 236, 238)

10) Tests (244-246)

11) Tests (242-246)

Arc: 225, 227

Arc: 233

Arc: 237

ignition processes [11]. At present, however, the body of data displayed in Figures 36 to 38 does not really point to any one electrode as being more important than the other. For example, reducing the length of the (positive) center electrode of configuration 4a to 4b also resulted in a reduction of energy consumed but, regrettably, Q was not constant in this experiment and the complementary case was not tested. It is thus premature to point to any one electrode from these results alone. If the anode processes are truly decisive for arcless ignition, then an enlarged anode surface should increase the capacity for electrochemical conversion before saturation occurs. Concurrently, the scatter in the experimentally determined values of E should become less prominent as the anode surface becomes greater. Indeed, the SEE listed in Table 7 seem to point in this direction, since omitting the smallest Q data point improves the regression of E versus Q .

Contrary to the good correlation between energy absorbed and electrode geometry discussed above, a relationship between the ignition delay, $t_{10\%}$, and geometry is more difficult to identify (Table 6, Figure 39). The reproducibility of the ignition delay time was for the most part rather poor (see Chapter 3.1.2). Nevertheless, a trend is visible in Figure 39; increasing Q will reduce $t_{10\%}$ when the center electrode is positive, but $t_{10\%}$ will increase when the center electrode is negative. Likewise, when plotted directly against the outer or inner electrode surface area, $t_{10\%}$ decreases with growing surface

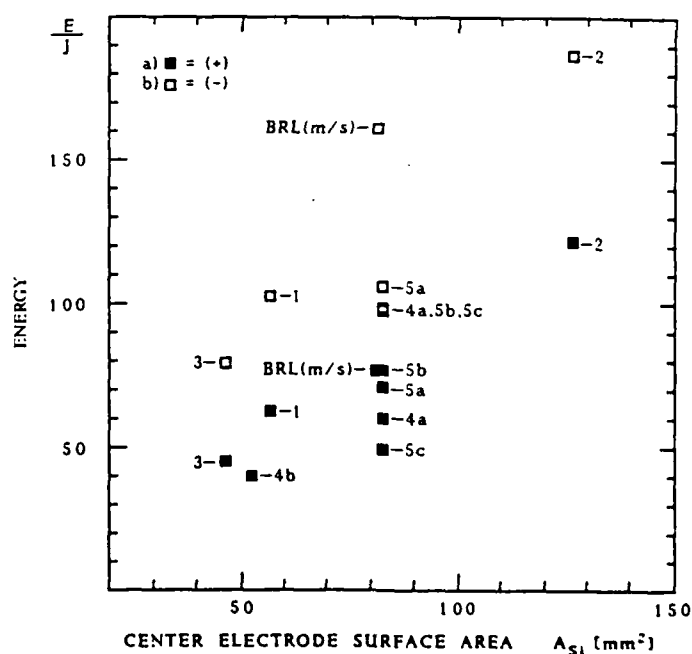


Fig. 36. Average energy absorbed versus surface area of center electrode; chamber volume 100 cm³; center electrode polarity: a) positive, b) negative.

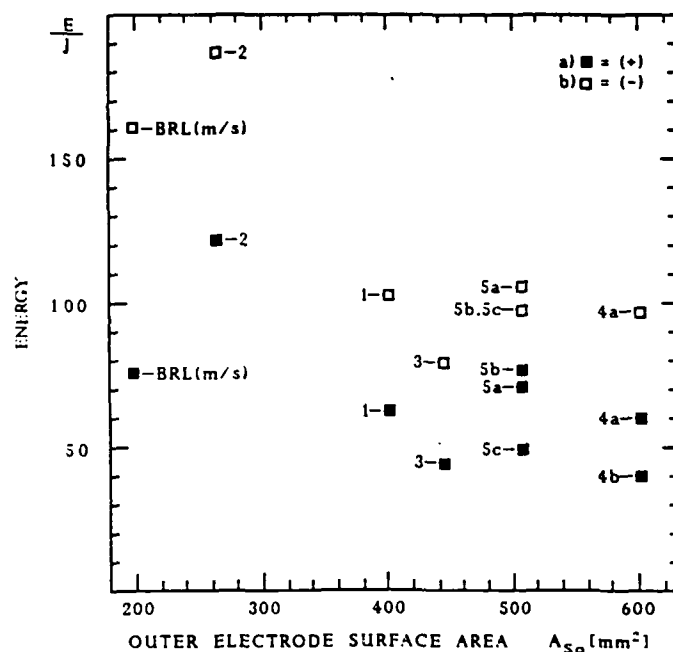


Fig. 37. Average energy absorbed versus surface area of outer electrode; chamber volume 100 cm^3 ; center electrode polarity: a) positive, b) negative.

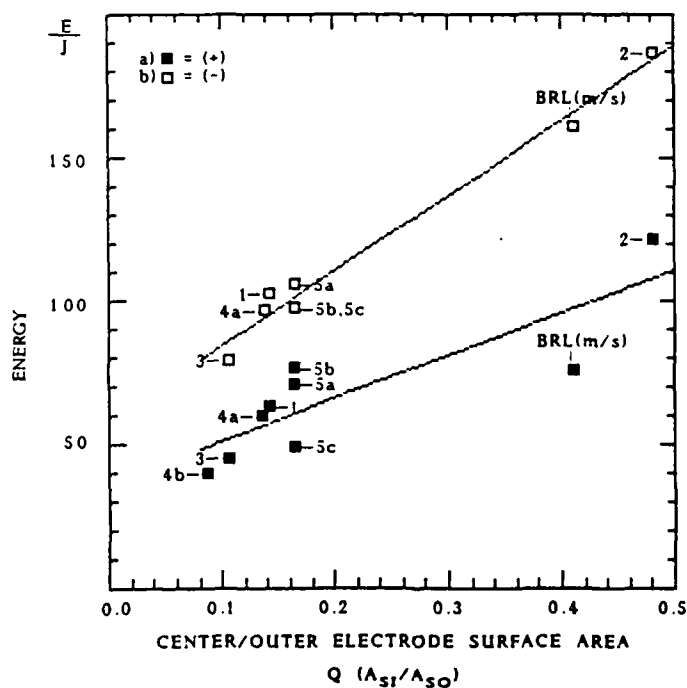


Fig. 38. Average energy absorbed versus surface area ratio Q ; chamber volume 100 cm^3 ; center electrode polarity: a) positive, b) negative

Table 7. Regression analysis E(Q); chamber volume 100 cm³; data from Figure 38

	F i g u r e		
	38(a)	38(b)	38(a') *
A ₀ [J]	36.1	58.6	30.6
A ₁ [J]	149.9	260.8	195.3
r	0.85	0.99	0.94
SEE [J]	± 13.7	± 5.6	± 9.8
n	9	8	8

n: number of points

SEE: Standard Error of Estimate: $x_{Y,X} = \sqrt{\frac{\sum (Y - \hat{Y})^2}{n-2}}$

$$\hat{Y} = A_0 + A_1 X$$

r: correlation coefficient

* Correlation between E and Q in 38(a) is improved by omitting Q = 0.141 (see 38(a')).

of a positive electrode (anode) and vice versa; the sole exception being that $t_{10\%}$ is insensitive to the area of the negative outer electrode, Figures 40 and 41.

The results shown in Figures 40 and 41 imply that the anode does actually dominate arcless ignition, especially for the case of a positive central electrode. Further, they support the validity of the assumption underlying the numerical optimization of the igniter geometry, namely that ignition will be favored in places of maximum field line density. For example, the outer negative electrode with low field line density plays no part in the ignition delays.

The final graph in this section, shown in Figure 42, attempts to correlate the energy consumption, and the ignition delay time with each other. The energy values in Figure 42 were calculated by taking into account the linear relationship of E versus U_{\max} (see Table 5, Figures 32 and 33). The appropriate U_{\max} values for each igniter in Table 3 were averaged; inserting the mean U_{\max} values into the corresponding regression equations (Table 5) gave the energy values plotted in Figure 42. The data points have been marked according to electrode polarity and igniter type. It seems relatively safe to conclude that the energy transfer found for a given igniter will increase with $t_{10\%}$ regardless of polarity. There is one exception: igniter configuration 3 exhibits an abnormally high ignition delay considering that the energy transfer is low; this is all the more puzzling as the same igniter fits well into the observed relationship

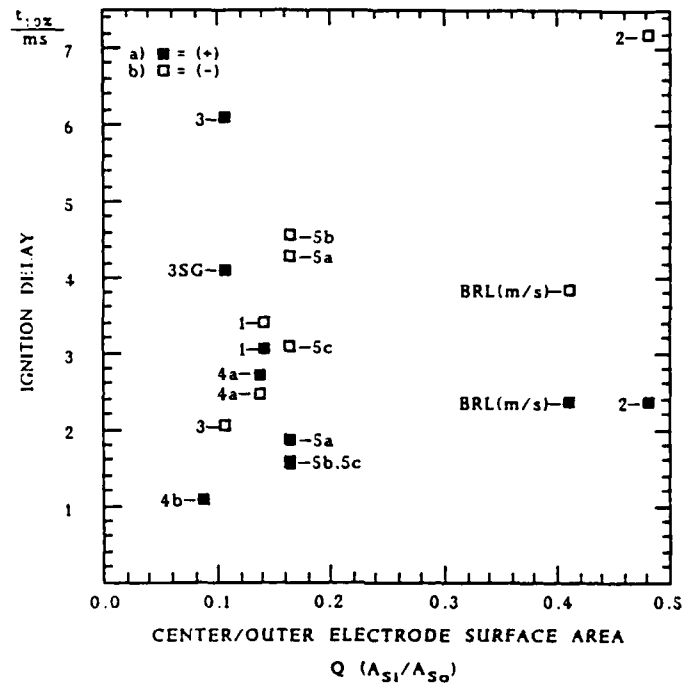


Fig. 39. Ignition delay time versus area ratio of electrodes; chamber volume 100 cm^3 ; center electrode polarity: a) positive; b) negative.

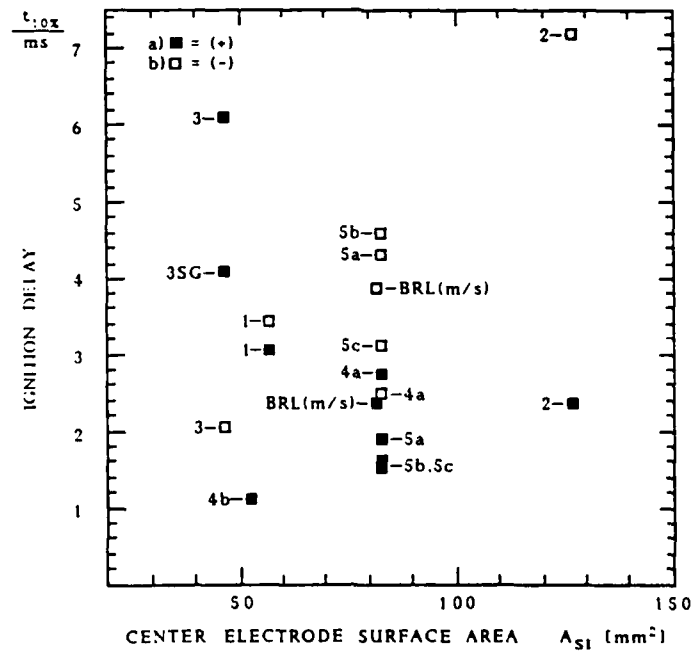


Fig. 40. Ignition delay time versus center electrode area; chamber volume 100 cm^3 ; center electrode polarity: a) positive, b) negative.

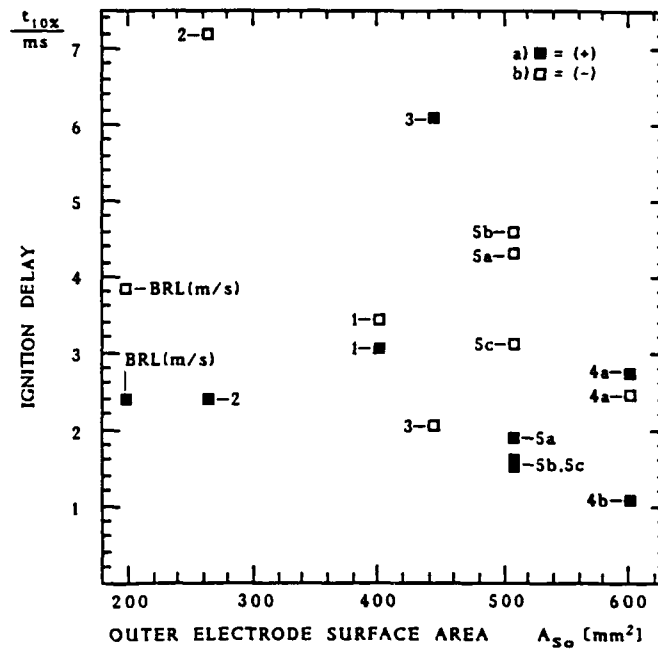


Fig. 41. Ignition delay time versus outer electrode surface area; chamber volume 100 cm³; center electrode polarity: a) positive, b) negative.

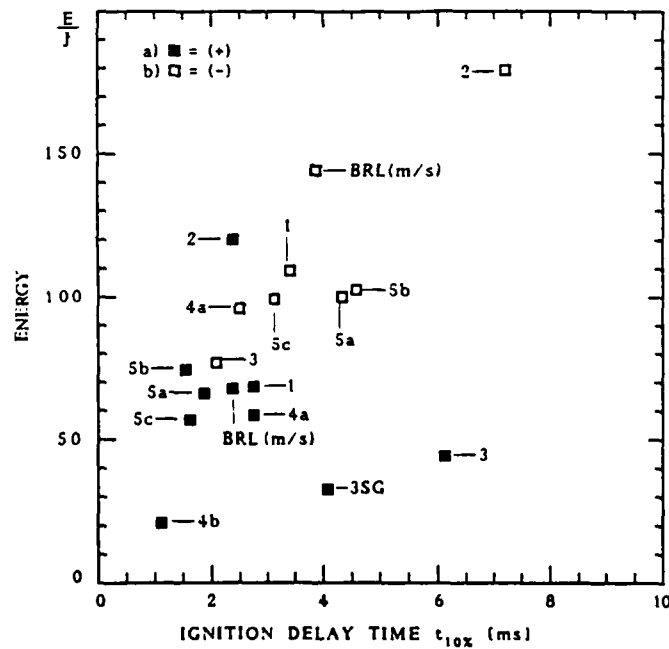


Fig. 42. Normalized energy consumption (see Table 5) versus ignition delay; chamber volume 100 cm³; center electrode polarity: a) positive, b) negative.

when the polarity is reversed. This might be due to the conical geometry of the liquid propellant reservoir in configuration 3, because more than for the other igniters, there is a sizeable amount of liquid propellant situated well away from the anode when the 'center' electrode is positive, but not when the 'outer' electrode is positive. Since the variations in geometry, as a whole, have not been altogether radical, this conclusion is tentative, at best, and will need further experimental validation.

3.1.6 Effect of Electrode Surface

As mentioned before, good reproducibility of ignition is highly desirable. At the present stage it seems that the significance of the controlling parameters, insofar as they are known, is far from well understood. One aspect that has not received very much attention in the past is the electrochemical behavior of the electrode itself. On the one hand, this is determined by the chemical nature of the electrode material; overpotentials, for example, play a crucial role in electrochemistry. The results obtained with the igniter EMI-AFB-3 fitted with an inert "Sigradur-G" glassy carbon electrode, as explained below, are a case in point. On the other hand, the surface roughness of an electrode at high field density can enhance or suppress arcing. For example, the field density is highest at surface discontinuities.

A glance at Table 6 reveals that the igniter configuration EMI-AFB-3, relatively low in energy consumption, required less energy after substituting the conventional stainless steel center electrode with an inert electrode of isotropic glassy carbon (3 SG). The material is manufactured by pyrolysis of a cross-linked polymeric resin. However, ignition was successful in two cases only (Table 3), these being the instances of highest U_{max} . What is more, ignition was not complete in the test (No. 253) with the lower energy. We presume that the energy transfer in the other tests was too low for ignition to occur. Increasing the size of the inner electrode should raise the energy above the threshold necessary for ignition. The mechanical stability of the two-piece electrode (see experimental section) was excellent.

It is apparent from the comparison of configurations 5a, 5b, and 5c in Figure 38 that the smoother electrode surface reduces the energy requirement of the igniter. There is an analogous trend towards shorter ignition delay times (Table 6). It is not clear whether or not this effect is due to the effective surface area alone, i.e., a rough surface has a larger effective surface area than a smooth one.

Scanning Electron Microscopy (SEM) and x-ray microanalysis were employed by Dynamit Nobel (DNAG) for analysis of the steel (Remanit 1.4401) electrode surface before and after the tests. Figure 43 shows SEM images of the center electrode tip as viewed from the top

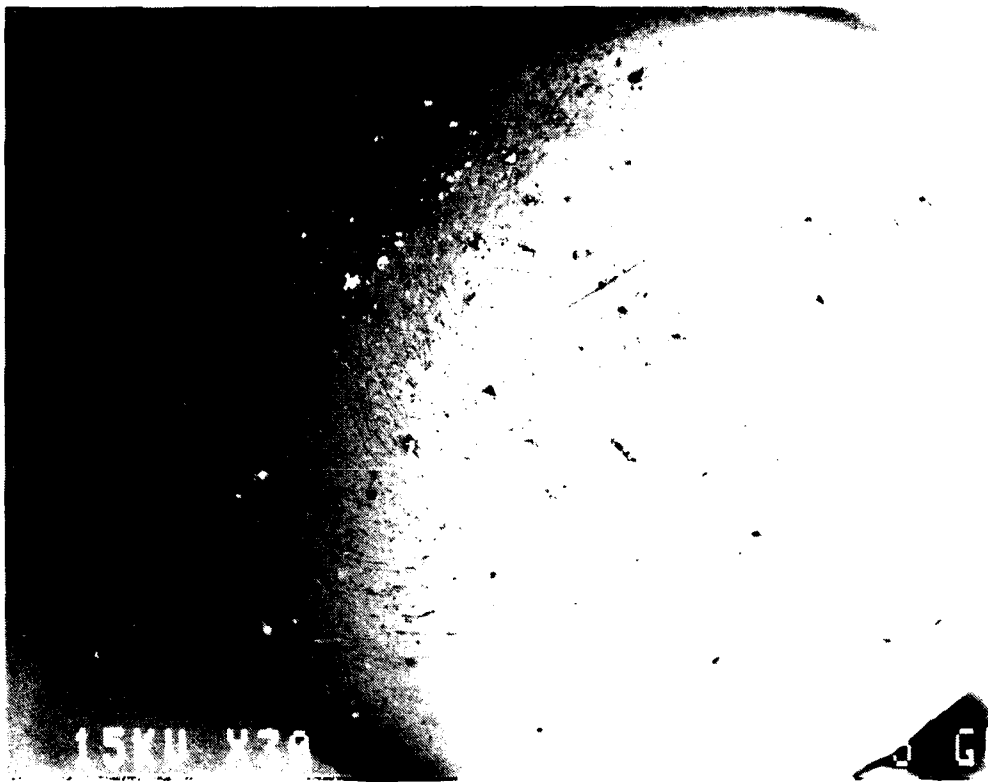


Fig. 43a. Image of backscattered electrons (SEM) from tip of center electrode before ignition (finishing: DIN 1000 grade sandpaper).

before and after ignition. The electrode surface has been worn down considerably. X-ray microanalysis showed that the surface deposits consist mainly of insulator and propellant residues. Analysis of the surface metal composition by x-ray microanalysis revealed that the Cr/Fe mass ratio changed from 0.53 before ignition to 1.29 after ignition. The immediate conclusion is that a more durable electrode material, a tungsten alloy or glassy carbon, for example, should be used in further work. As a matter of fact, the results in general point out the need for chemically and mechanically more stable materials in igniter construction.

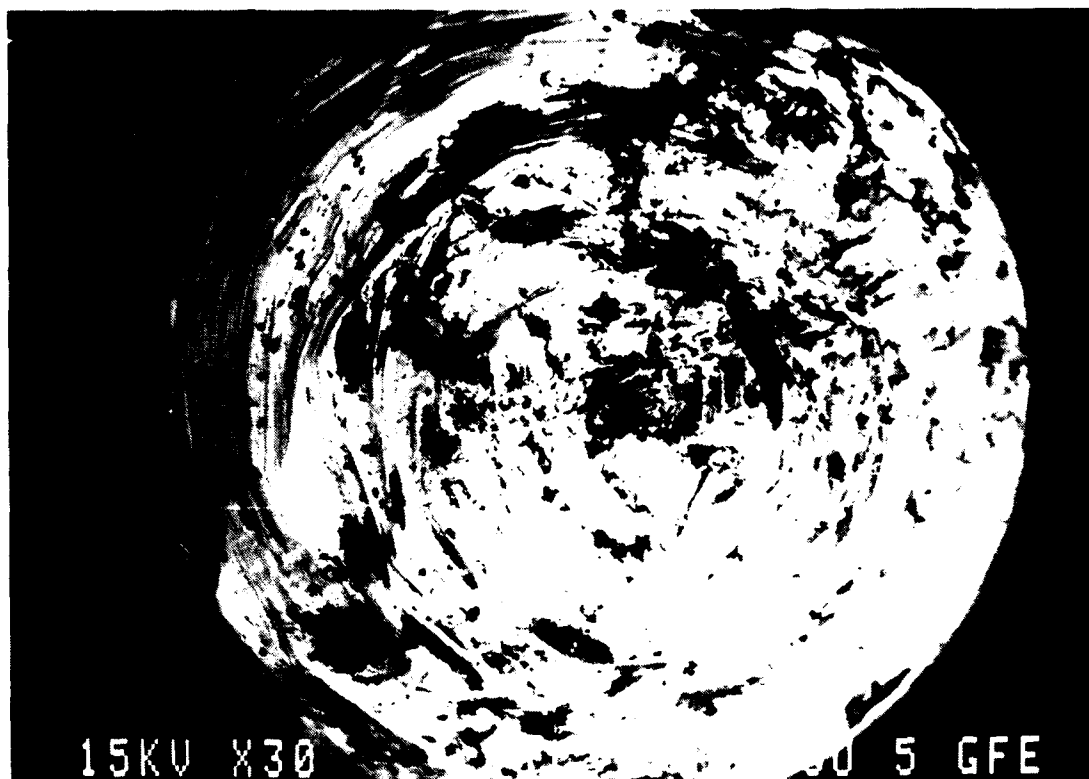


Fig. 43b. Image of backscattered electrons (SEM) from tip of center electrode after ignition.

3.2 EMI-AFB Ignition Test Fixture 2

The ignition test fixture 2 was employed for basic ignition studies with LGP 1846. The test fixture was shown schematically in Figures 20 and 21. The electrode shapes are depicted in Figure 22. The least arcing problems were encountered using the plate-plate or plate-sphere geometry; the field strength was varied by changing the size of the electrode gap. The original fill volume of 7 cm³ of liquid propellant contained so much energy that mechanical failure of the electrode assembly was the rule rather than the exception during the first test series. Subsequently a teflon insert was placed in the liquid propellant reservoir thus reducing the fill volume to about 3 cm³. Nevertheless, often enough liquid propellant was still forced through the small gaps between insulator and steel. These mechanical problems, in turn, had adverse effects on reproducibility.

One finding of the tests carried out with test fixture 2 was the wide range and irreproducibility of the ignition delay time, $t_{10\%}$. Values between 3 ms and 1.5 min were observed. Interestingly,

however, the phenomena recorded in the transmission as well as the emission modes with a 4 kHz framing rate high-speed film were considerably more uniform in their time scales. The visible processes invariably began within the first millisecond after circuit closure ($t = 0$). To a first approximation the sequence of events was identical in all filmed tests, the magnitude of emission/absorption, however, did vary. The sequence of events was unchanged regardless of whether or not the chemical reactions culminated in genuine ignition or mere decomposition of the liquid propellant. Moreover, the magnitude of events could not be correlated either to ignition as such nor to the ignition delay.

A sequence of transmission photographs taken during ignition of LGP 1846 between two plate electrodes are shown in Figure 44. A diffuse opaque zone appears within the first 0.25 ms after circuit closure at the cathode. This is certainly unexpected in view of the earlier results by Carleton et al. [11], obtained with platinum electrodes, which point to the anode as the locus for the relevant ignition chemistry. Judging from our photographs, however, we would not go so far as to dispute the Carleton et al. findings [11].

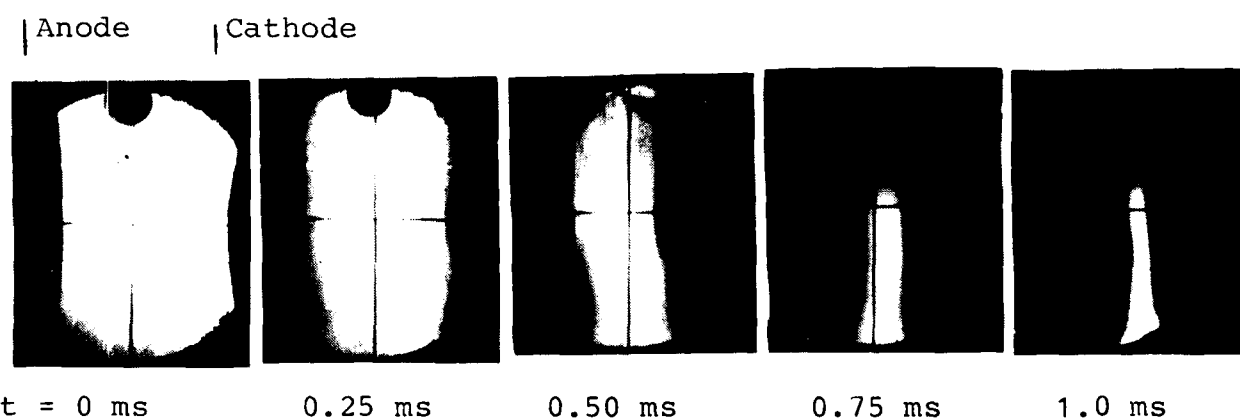


Fig. 44. High-speed (4 kHz) transmission photography of ignition of LGP 1846.

The next frame shows a diffuse zone growing from the anode and in the following frames the opaque zone at the anode grows at a faster pace than at the cathode. In this test, $t_{10\%}$ was 30 ms.

It should be noted that an air bubble present near the top of the liquid propellant volume in the first frames is completely absorbed by the third frame (0.5 ms). There is some subsequent blackening of the film in the area of the bubble, but this is apparently overwhelmed by the material growing from the anode. This was the only test during which such a bubble was observed; thus, the ignition delay is not seen as being connected to its appearance.

The representative sequence of emission photographs in Figure 45 basically shows features similar to the preceding transmission photographs. Emission also begins first at the cathode ultimately being superceded by the generally much stronger emission from the anode. This test showed the weakest emission phenomena of all recordings, the ignition delay was 80 ms. Again, the magnitude of emission could not be correlated to successful/unsuccessful ignition.

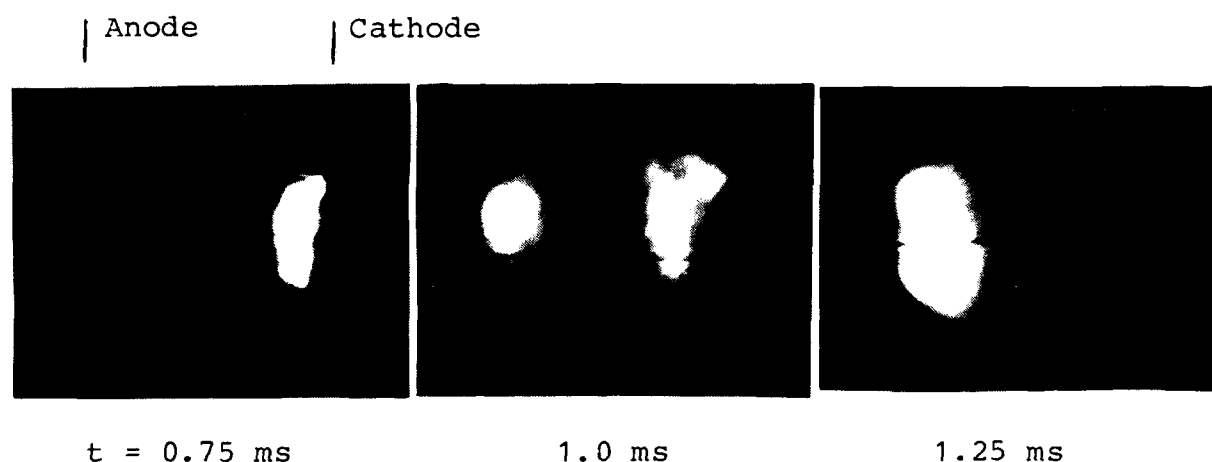


Fig. 45. High-speed (kHz) emission photography of ignition of LGP 1846.

The emission of light disappeared well before ignition actually occurred. Further, the flow of current was always over at about 0.8 ms just as with the igniters tested in the ignition test fixture 1. The short duration of current flow together with the long ignition delays suggest an electrochemically/ohmic heating induced chemical mechanism for ignition. The reasons for the poor reproducibility of ignition in the EMI-AFB test fixture 2 are unclear; possibly a chemically inert and certainly a mechanically more stable test chamber than the one available would be required to investigate further.

3.3 30-mm RLPG Test Firings

A main objective of this research project was to obtain igniter energy effluxes capable of starting the regenerative process and producing self-sustained combustion in a regenerative liquid propellant gun.

A 30-mm RLPG simulator with an initial combustion chamber volume of 20 cm³ and showerhead injection [18] was chosen as a first test weapon. The igniter was the EMI-AFB-3 type because of its low energy

consumption and a relatively easy machinability. The vent orifice diameter was 1.5 mm, and the center electrode polarity positive. LGP 1846 was loaded in the igniter and an 80%/20% (by weight) nitro-methane/methanol mixture was used in the liquid propellant reservoir.

Figure 46 shows the $p(t)$ history in the combustion chamber for a test in which the injector "nozzle" diameter was 2.5 mm. Electrical interference (HF signal) was observed on the $p(t)$ curve between 0 ms and 1.5 ms. Figures 47 and 48 also show comparative $p(t)$ plots recorded in the combustion chamber. For comparison, the test shown in Figure 47 was performed using 2.8 g of black powder as igniter. In Figure 48 initiation, as with Figure 46, was once more by arcless electrical ignition of LGP 1846. The injector holes used for these last two tests had a diameter of 1.5 mm, which throttled the combustion so that burning was incomplete and the pressure buildup reduced relative to the test shown in Figure 46. It is interesting to note that the powder igniter causes a steeper initial pressure buildup (Figure 47) than the liquid propellant igniter (Figure 48). The final performance, however, is virtually the same in both cases. The projectile velocities, for example, were 415 and 430 m/s, respectively.

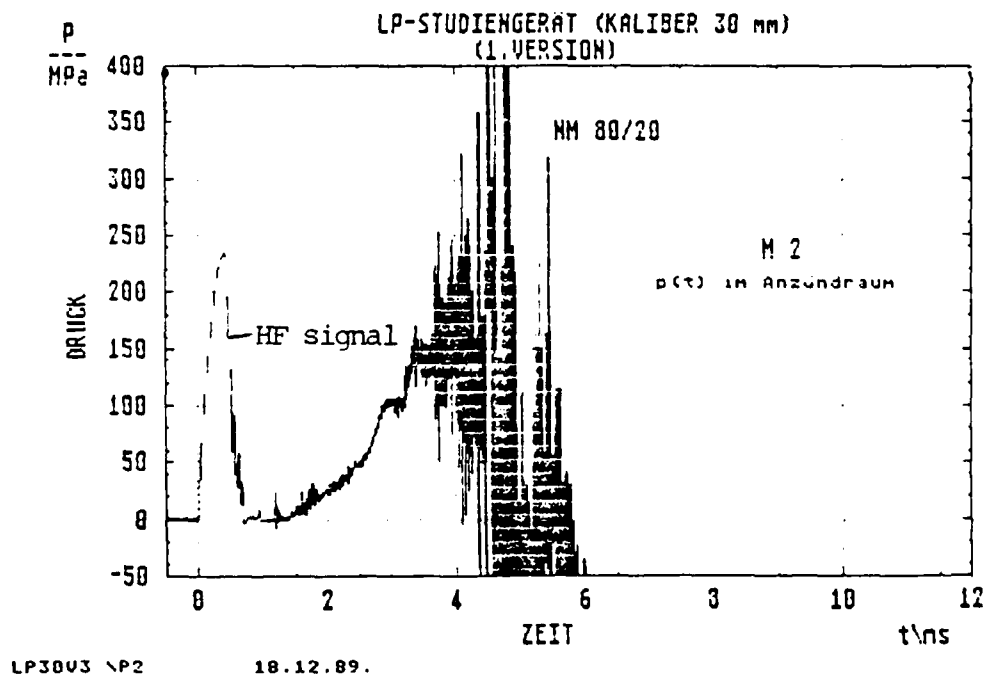


Fig. 46. Pressure versus time; 30-mm RLPG, showerhead injection (vent diameter = 2.5 mm); ignition: electrical; 1.9 cm³ LGP 1846; LP reservoir: N/M 80/20, 59 cm³.

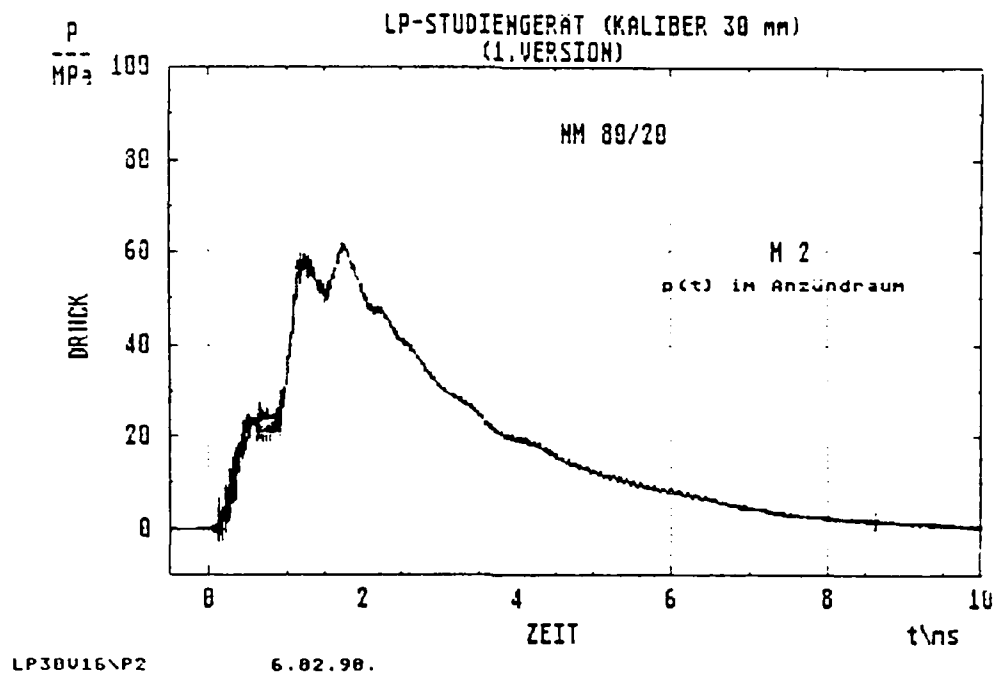


Fig. 47. Pressure versus time; 30-mm RLPG; showerhead injection (vent diameter = 1.5 mm); ignition: 2.8 g black powder; LP reservoir: N/M 80/20, 59 cm³.

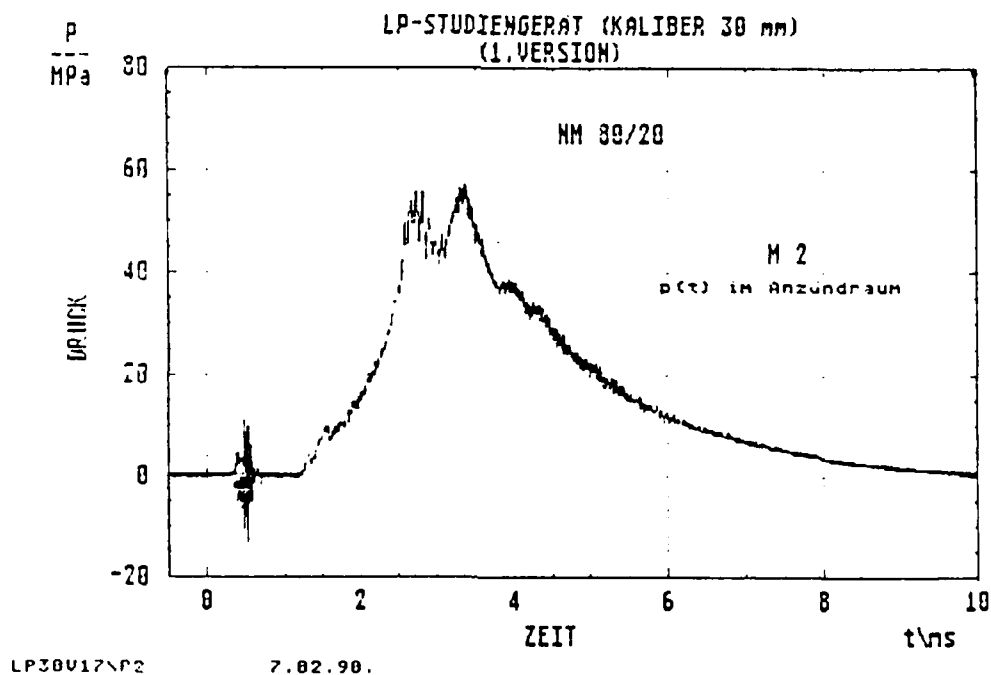


Fig. 48. Pressure versus time; 30-mm RLPG; showerhead injection (vent diameter = 1.5 mm); ignition: electrical; 1.9 cm³ LGP 1846; LP reservoir: N/M 80/20, 50 cm³.

Recent modifications of the showerhead injector have considerably reduced pressure fluctuations so that the simulator may be tested with LGP 1846 in both igniter and reservoir in the near future. Moreover, the scaling up of ignition to larger calibers is now planned. One basic strategy for scaling igniter performance to large calibers will be to deploy multiple igniters in parallel. Further enlargements of the cavity size of 1.9 cm^3 is unlikely due to the mechanical stresses expected in such an enlarged system. As has already been pointed out, more durable materials are needed for the projected improvement of the igniters.

3.4 IR Spectroscopy

Preliminary measurements of the IR-emission accompanying liquid propellant combustion were made during the 30-mm RLPG test firings. The full spectral range of 0.64 to $5.32 \text{ }\mu\text{m}$ was scanned once every millisecond. A series of spectra taken from one of the tests is shown in Figure 49 and a reference spectrum of combusting $3\text{H}_2/\text{O}_2$ in Figure 50. The sharp peaks at the center and edges of the spectral range are due to incomplete calibration as a result of a poor optical setup. For example, the aperture of the available windows was too small for the sapphire fiber optics. Given more time, these pseudo-signals are removable in a straightforward fashion, especially the overlap of the signals from the relatively short IR wave length ($<2.6 \text{ }\mu\text{m}$) and the relatively long IR wavelen ($>2.42 \text{ }\mu\text{m}$) halves of the spectrum is, normally, near perfect.

The main features in Figure 49 are caused by H_2O bands; this is an expected result. The separation of the bands, however, is less pronounced for the liquid propellant case than for the $3\text{H}_2/\text{O}_2$ mixture. This can be traced to emissions of carbon containing species in the combustion mixture. The broad absorption profile sloping downward from 1.4 to $4 \text{ }\mu\text{m}$ in Figure 49d is most likely caused by blackbody radiation from flow-borne carbon particles. The analytical potential of the method is illustrated in Figure 51. Different selected wavelengths show characteristic intensity versus time histories and thus permit access to information on the reaction kinetics.

The spectral resolution is, at present, limited by the available gratings. For the initial trial runs, a broad spectral range was preferred over high spectral resolution. Once appropriate wavelengths for the analysis of liquid propellant combustion dynamics have been selected, appropriate gratings will be easy to obtain. It should be noted that the spectral resolution must, of course, suffer from temperature and pressure broadening, when compared to measurements at atmospheric pressure. At elevated pressure and temperature some a priori modeling will be inevitable. Any theoretical method, however sophisticated, will not be entirely successful at mitigating signal broadening, thus detection of trace quantities of exotic species by IR spectroscopy presents a formidable problem better

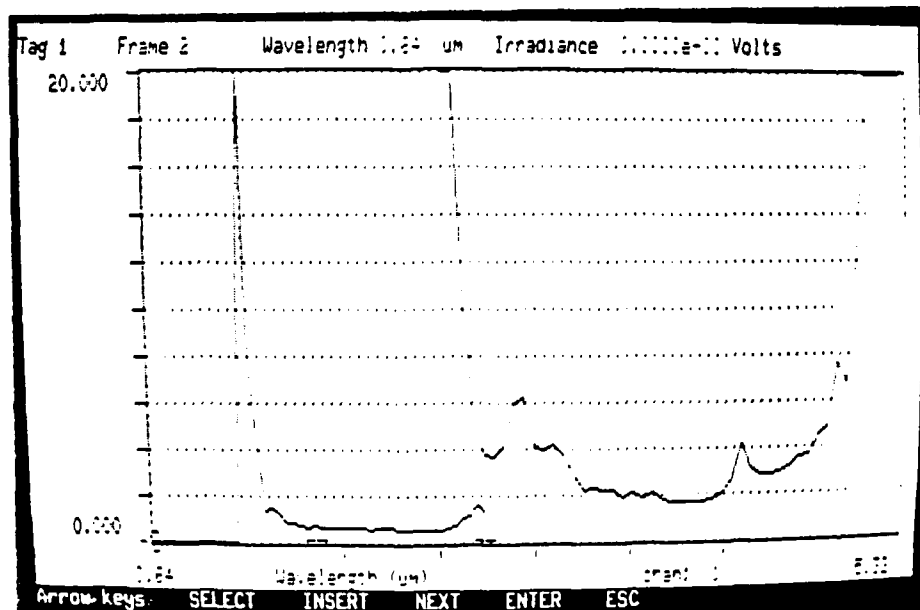


Fig. 49a. IR spectrum taken during firing of 30-mm RLPG; emission intensity versus wavelength [μm]; time after trigger: 2 ms.

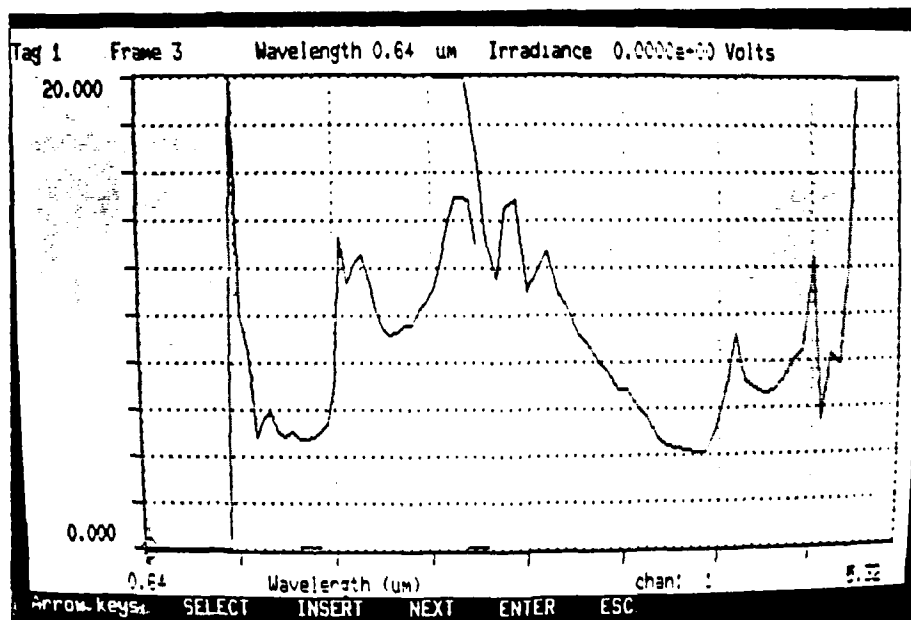


Fig. 49b. IR spectrum taken during firing of 30-mm RLPG; emission intensity versus wavelength [μm]; time after trigger: 3 ms.

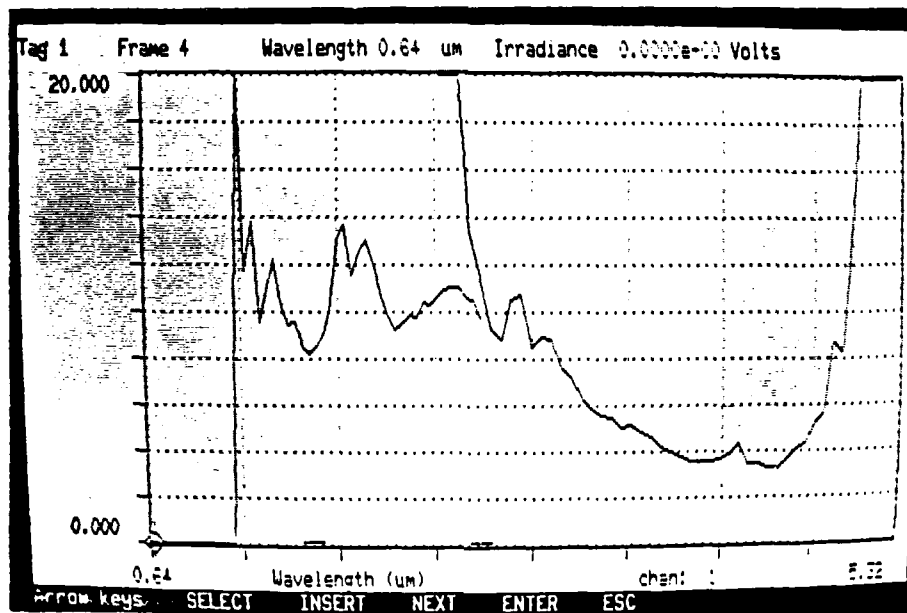


Fig. 49c. IR spectrum taken during firing of 30-mm RLPG; emission intensity versus wavelength [μm]; time after trigger: 4 ms.

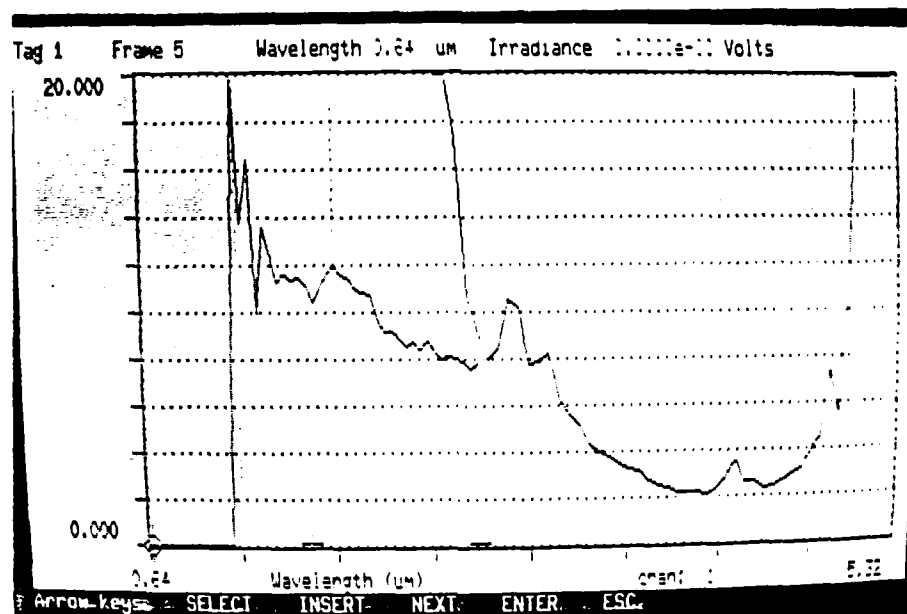


Fig. 49d. IR spectrum taken during firing of 30-mm RLPG; emission intensity versus wavelength [μm]; time after trigger: 5 ms.

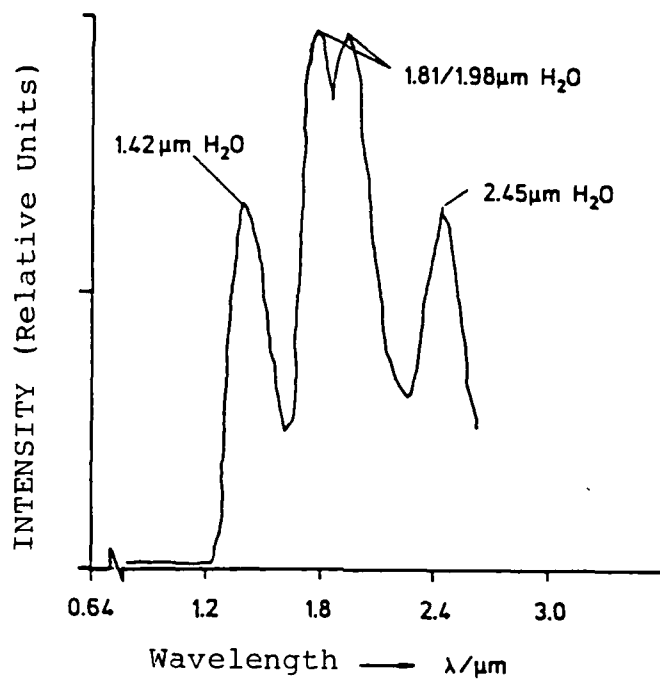


Fig. 50. IR spectrum of combustng $3\text{H}_2/\text{O}_2$ diluted by 8He.

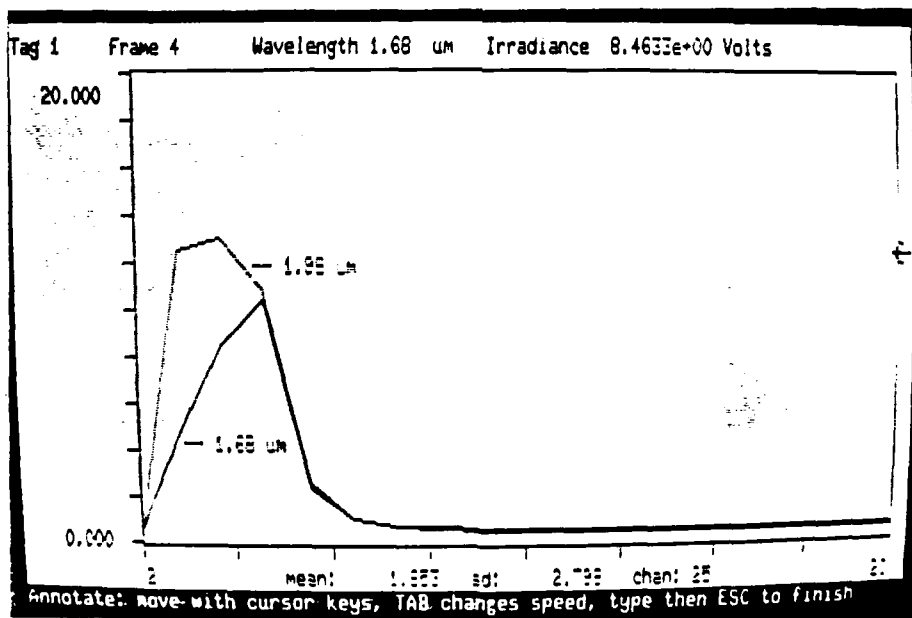


Fig. 51a. Intensity versus time; $\lambda = 1.68/1.98\mu\text{m}$. (One time frame is about 1 ms; $t = 2$ to 20 ms).

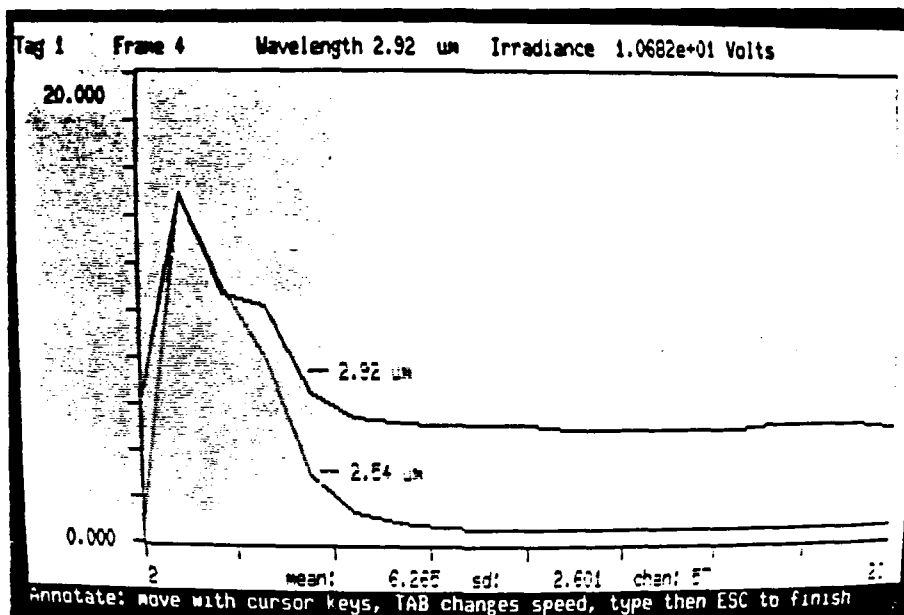


Fig. 51b. Intensity versus time; $\lambda = 2.54/2.92 \mu\text{m}$. (One time frame is about 1 ms; $t = 2$ to 20 ms).

resolvable by sophisticated gas chromatographic/mass spectrometric (GC/MS) techniques. The big advantage of the IR spectrometer is the fact that it allows nonintrusive time-resolved measurements with a minimum of effort.

4. CONCLUSIONS

The feasibility of arcless ignition of LGP 1846 was studied using vented chambers, and it was demonstrated in a caliber 30-mm RLPG simulator. The igniter design consists of a center electrode separated from a more or less conically shaped vented outer electrode by a hollow cylindrical insulator. The design is considered suitable for practical application. As far as scaling up to larger calibers is concerned, the simplest strategy would be to build an enlarged version of the 1.9 cm^3 igniter. The main difficulties with this approach are the unknown ignition scaling parameters and the mechanical stability of the component parts, which may not withstand the stresses generated by larger volumes of liquid propellant charges. It may instead be easier to use an arrangement of a yet to be specified number of igniters of the present type and size working in parallel to achieve the necessary performance. Another approach is a staging process in which the liquid propellant in the first stage is ignited electrically and subsequent stages are ignited from the reaction products and heat released from the preceding stage. The use of new and more durable materials for the insulator and elec-

trodes might push up further the limit of the manageable liquid propellant quantity. High strength non-metallic composites available on the market today are especially promising as insulator and shock absorbing materials. Tungsten alloy or glassy carbon are potential electrode materials.

Simple electrostatic theory has proven to be a valuable tool for the optimization of the electrode and cavity geometries. Computer aided numerical calculations yielded an improved electrode geometry, which absorbs less electrical energy and requires less charge voltage than the earlier designs. Apart from the overall geometry, the energy consumption of the igniter is determined mainly by polarity, electrode surface area, anode/cathode area ratio, and charge voltage. An increase in the liquid propellant confinement by reducing the vent size will act to reduce the ignition delay.

High-speed emission and transmission films taken during the ignition process indicate a chemical ignition mechanism. Ohmic heating and/or electrochemical conversion are not in themselves sufficient to force ignition by way of the primary decomposition products. Rather, the very long ignition delays encountered with the EMI-AFB ignition test fixture 2 imply that additional reactive intermediates are necessary.

Scanning electron microscopy (SEM) and x-ray microanalysis show that ignition is affected by the chemical and physical characteristics of the electrode surface. Corrosion and wear of the steel presently used were considerable. A uniformly smooth surface reduces ignition delay and energy transfer to the liquid propellant.

Preliminary results of IR spectrometric monitoring of combusting liquid propellant demonstrate the applicability of the method as a diagnostic tool. The species resolution is lower than that of Gas Chromatography/Mass Spectrometry, but temporal resolution is more easily and non-intrusively achieved.

ACKNOWLEDGEMENT

The ignition work described herein has been made possible through the support of the U. S. Government and its United States Army Research, Development and Standardization Group (UK), USARDSG(UK), London, England, the Ballistic Research Laboratory (BRL), Aberdeen Proving Ground, Maryland, USA, the Dynamit Nobel AG, as well as the German Ministry of Defense (MOD), Rue VII 7, Bonn. We thank Dr. Roy Reichenbach of the USARDSG(UK), Dr. Walter F. Morrison and Mr. John D. Knapton of BRL and the Dynamit Nobel AG for their support. Also, we wish to express our gratitude to Mrs. Erika Messner of EMI for typing and organizing the manuscript and to Messrs. Otto Wieland and Rolf Roschig who carried out substantial parts of the experimental work at the Ernst-Mach-Institut.

5. REFERENCES

- [1] F.J. Weinberg, "Plasma Jets in Combustion", Imperial College of Science and Technology, C45/33, IMechE, 1983, pp. 65-72.
- [2] A.J. Lee and F.J. Weinberg, "A Novel Ignition Device for the Internal Combustion Engine", Nature, Vol. 311, 738 (1984).
- [3] I.M. Vince, C. Vovelle, and F.J. Weinberg, "The Effect of Plasma Jet Ignition on Flame Propagation and Sooting at the Rich Limit of Flammability", Combustion and Flame, Vol. 57, 105 (1984).
- [4] J. DeSpirito and J.D. Knapton, "LP Ignition and Igniter Testing", Proc. DEA-G-1060 Germany/United States Workshop on Liquid Propellant Gun Technology, Düsseldorf/Unterlöss, FRG, 1988.
- [5] G. Klingenberg, H. Rockstroh, J.D. Knapton, J. DeSpirito, and H.-J. Frieske, "Electrical Ignition of HAN-Based Liquid Propellants", Proc. 11th International Symposium on Ballistics, Brussels, Belgium, 1989.
- [6] J. DeSpirito, J.D. Knapton, and I.C. Stobie, "Progress on Electrical Ignition of Liquid Gun Propellants for Application in Regenerative Liquid Propellant Guns", Proc. 24th JANNAF Combustion Meeting, Monterey, CA, 1987.
- [7] W.F. Morrison, J.D. Knapton, and M.J. Bulman, "Liquid Propellant Guns", in Gun Propulsion Technology, L. Stiefel (Ed.), Progress in Astronautics and Aeronautics, Vol. 109, Chapter 13, p. 413, AIAA, Washington, D.C., 1988.
- [8] G. Klingenberg, J.D. Knapton, and W.F. Morrison, "Review on Liquid Propellant Ignition Studies", Fraunhofer-Institut für Kurzzeitdynamik, Ernst-Mach-Institut, Weil am Rhein, FRG, EMI-AFB Report V 7/83, 1983.
- [9] M.M. Decker, N. Klein, E. Freedman, C.S. Leveritt, and J.Q. Wojciechowski, "HAN-Based Liquid Gun Propellants: Physical Properties", U.S. Army Ballistic Research Laboratory, Aberdeen Proving Ground, MD, Report BRL-TR-2864, 1987.
- [10] C.G. Irish, "Modeling Formative Phase of Liquid Propellant Spark Ignition Systems - Theoretical Prediction of Thermal and Electrical Behavior", Naval Ordnance Station, Indian Head, MD, NOS Report 47, 1977.
- [11] F.B. Carleton, G. Chevion, N. Klein, and F.J. Weinberg, "Optical Study of Electrical Discharge - Liquid Propellant Interaction", U.S. Army Ballistic Research Laboratory, Aberdeen Proving Ground, MD, Report BRL-TR-2706, 1986.

- [12] N. Klein, R.A. Sasse, R.L. Scott, and K.E. Travis, "Thermal Decomposition of Liquid Monopropellants", U.S. Army Ballistic Research Laboratory, Aberdeen Proving Ground, MD, Report BRL-TR-1970, 1977.
- [13] J.J. Kaufman and W.S. Koski, "Study of the Hydroxylammonium-nitrate-Isopropylammoniumnitrate Reaction", Final Report Contract DAAG29 76 C 0029, John Hopkins University Baltimore, MD, 1980.
- [14] N.A. Messina, "Thermal Decomposition Studies of HAN-Based Liquid Monopropellants", Proc. 22nd JANNAF Combustion Meeting, 1985.
- [15] N. Klein, "Liquid Propellants for Use in Guns", in Gun Propulsion Technology, L. Stiefel (Ed.), Progress in Astronautics and Aeronautics, Vol. 109, Chapter 14, p. 473, AIAA Washington, D.C., 1988.
- [16] J.D. Knapton, I.C. Stobie, R.H. Comer, O.L. Henry, B.D. Bensinger, and L. Stansbury, "Charge Design Studies for a Bulk-Loaded Liquid Propellant Gun (U)", U.S. Army Ballistic Research Laboratory, Aberdeen Proving Ground, MD, Report ARBTL-TR-02127, 1978.
- [17] H.-J. Frieske, "Elektrische Anzündung von flüssigen Rohrwaffentreibmitteln", Dynamit Nobel AG, Köln, FRG, Report ES-Abt. GZ, 1988.
- [18] G. Klingenberg, H. Haas, and O. Wieland, "LP-Studiengerät vom Kaliber 30 mm - Eigenbau EMI-AFB", Fraunhofer-Institut für Kurzzeitdynamik, Ernst-Mach-Institut, Weil am Rhein, FRG, EMI-AFB Report 25/88, 1988.
- [19] G. Klingenberg, H. Rockstroh, and U. Steffens, "Elektrische Anzündung von Nitromethan/Methanol-Mischungen", Fraunhofer-Institut für Kurzzeitdynamik, Ernst-Mach-Institut, Weil am Rhein, FRG, EMI-AFB Report 15/89, 1989.
- [20] G. Klingenberg, H.-J. Frieske, and H. Rockstroh, "Elektrische Anzündung von monergolen flüssigen Rohrwaffentreibmitteln", Fraunhofer-Institut für Kurzzeitdynamik, Ernst-Mach-Institut, Weil am Rhein, FRG, EMI-AFB Report 8/88, 1988, p. 63.